Efficient Computer Program EPAS-J1 for Calculating Stress Intensity Factors of Three-Dimensional Surface Cracks

March 1982

日 本 原 子 力 研 究 所

Japan Atomic Energy Research Institute

Efficient Computer Program EPAS-J1 for Calculating Stress Intensity Factors of Three-dimensional Surface Cracks

Noriyuki Miyazaki, Takayuki Watanabe* and Genki Yagawa**

Division of Reactor Safety, Tokai Research Establishment
Japan Atomic Energy Research Institute
Tokai-mura, Naka-gun, Ibaraki-ken

Abstract

A finite element computer program EPAS-J1 was developed to calculate the stress intensity factors of three-dimensional cracks. In the program, the stress intensity factor is determined by the virtual crack extension method together with the distorted elements allocated along the crack front. This program also includes the connection elements based on the Lagrange multiplier concept to connect such different kinds of elements as the solid and shell elements, or the shell and beam elements. For the structure including three-dimensional surface cracks, the solid elements are employed only at the neighborhood of a surface crack, while the remainder of the structure is modeled by the shell or beam elements due to the reason that the crack singularity is very local. Computer storage and computational time can be highly reduced with the application of the above modeling technique for the calculation of the stress intensity factors of the three-dimensional surface cracks, because the three-dimensional solid elements are required only around the crack front.

Several numerical analyses were performed by the EPAS-J1 program. At first, the accuracies of the connection element and the virtual crack extension method were confirmed using the simple structures. Compared with other techniques of connecting different kinds of elements such as the tying method or the method using anisotropic plate element, the present connection element is found to provide better results than the others. It is also found that the virtual crack extension method provides the accurate stress intensity factor. Furthermore, the results are also presented for the stress intensity factor analyses of cylinders with longitudinal or circumferential surface cracks using the combination of the various kinds of elements together with the connection elements.

---

* Century Research Center Corporation
** Department of Nuclear Engineering, Faculty of Engineering, University of Tokyo

3次元物体中の表面き裂の応力拡大係数解析のための効率的なプログラムEPAS-J1について

日本原子力研究所東海研究所安全工学部

宮崎則幸・渡辺隆之[*]・矢川元基[**]

要　　　旨

　3次元物体中の表面き裂の応力拡大係数を解析するために有限要素法プログラム EPAS-J 1 を開発した．このプログラムでは，き裂縁に沿っては移動節点要素を配置し，仮想き裂進展法により応力拡大係数を求めている．また EPAS-J 1 プログラムは中実要素と板殻要素，及び板殻要素とはり要素とを結合するために，ラグランジュ乗数法に基づいた結合要素も含んでいる．表面き裂を含む構造物では，き裂の特異性は局所的であるため，中実要素を表面き裂近傍のみに配置し，その他の領域は板殻要素あるいははり要素によりモデル化できる．3次元中実要素はき裂の近傍以外は必要ないので，表面き裂の応力拡大係数の計算にこのようなモデル化を用いることにより，計算機の記憶容量及び計算時間の大幅な低減ができる．

　EPAS-J 1 プログラムを用いて幾つかの数値解析を実施した．最初に，簡単な構造モデルを用いて，結合要素と仮想き裂進展法の精度を検討した．線形拘束方程式を用いる方法あるいは結合要素として異方性板要素を用いる方法等と比べて，EPAS-J 1 プログラムで用いている結合要素は良好な結果を与えることが分かった．また，仮想き裂進展法も精度の良い結果を与えることも分かった．さらに，結合要素により異種要素を結合するモデル化を用いた，軸方向あるいは周方向の表面き裂がある円筒の応力拡大係数解析の結果も示した．

　 * 　センチュリリサーチセンター（株）
** 　東京大学工学部原子力工学科

Contents

目 次

1. Introduction

The fracture mechanics analysis of the surface cracks existing in pressure vessels and piping is important in assessing the structural integrity of nuclear power plants. Such an analysis, however, requires considerable computer storage and computational time, because the three-dimensional analysis must be carried out to obtain the local stress and strain distributions near the surface crack. The substructure method has been used to deal with the finite element structural analysis of a large scale three-dimensional structure. Reynen[1], Broekhoven[2], Hall *et al.*[3], and Bergan and Aamodt[4] used this method to obtain the stress intensity factors of the three-dimensional cracks. It is doubtful, however, whether the substructure method is more economical in computational cost than any other methods or not, because it requires the inverse of the stiffness matrix of each substructure to eliminate the degrees-of-freedom in the substructure. Yagawa *et al.*[5] developed the finite element computer program EPAS (= Elastic-Plastic Analysis System) for economical and efficient calculation of the local three-dimensional elastic-plastic behavior. This program has the connection elements based on the Lagrange multiplier concept to combine such different types of elements as the solid and shell elements or the shell and beam elements. Afterwards, the EPAS program was so modified as to be used to analyze the stress intensity factors of the three-dimensional cracks. This modified program is named EPAS-J1 (= Elastic-Plastic Analysis System, JAERI version 1). Various methods have been proposed to obtain the stress intensity factor by the finite element method as shown in ref. (6). The EPAS-J1 program uses the virtual crack extension method[7][8] to obtain the stress intensity factor, because this method can be easily incorporated into the existing finite element program and provides comparatively accurate stress intensity factor. In this code, the distorted elements[9][10][11] are allocated along the crack front to represent the stress singularity near the crack front. For the structure including three-dimensional surface cracks, the solid elements are employed only at the neighborhood of the surface crack, while the remainder of the structure is modeled by the shell or beam elements due to the reason that the crack singularity is very local. Thus, computer storage and computational time could be reduced considerably with the application of the above modeling for calculation of the stress intensity factors of the three-dimensional cracks, because the three-dimensional solid elements are required only near the crack front.

In the report, Chapter 2 describes the theoretical background of the connection elements and the virtual crack extension method. Several numerical examples are presented in Chapter 3. In this chapter, the accuracies of the connection element and the virtual crack extension method are confirmed. The stress intensity factor analyses using connection elements are also included in this chapter. The conclusions are described in Chapter 4.

2. Theoretical Background of the EPAS-J1 Program

2.1 Derivation of Finite Element Equilibrium Equation

2.1.1 Basic Equations and their Variational Form

Consider a general three-dimensional problem in solid mechanics. With respect to a system of orthogonal Cartesian coordinate x_i, i = 1, 2, 3, the governing equations of the problem can be written in the incremental form in the small displacement theory as follows:

$$\Delta\sigma_{ij,j} + \Delta\overline{P}_i = 0 \qquad \text{(in } V) \qquad (2.1.1)$$

$$\Delta\epsilon_{ij} = \frac{1}{2}(\Delta u_{i,j} + \Delta u_{j,i}) \qquad \text{(in } V) \qquad (2.1.2)$$

$$\Delta\sigma_{ij} = E^{ep}_{ijk\ell}\,\Delta\epsilon^{ep}_{k\ell} + G^{ep}_{ij}\,\Delta T \qquad \text{(in } V) \qquad (2.1.3)$$

$$\Delta u_i = \Delta\overline{u}_i \qquad \text{(on } S_u) \qquad (2.1.4)$$

and

$$\Delta T_i = \Delta\overline{T}_i \qquad \text{(on } S_\sigma) \qquad (2.1.5)$$

with

$$\Delta T_i = \Delta\sigma_{ij}n_j \qquad \text{(on } S) \qquad (2.1.6)$$

where σ_{ij}, ϵ_{ij}, u_i and P_i are stresses, strains, displacements and body forces, respectively. Δ denotes an increment and $(^-)$ implies prescribed quantities. V is the volume occupied by the body. S_u and S_σ are the surface S of the body V in which the displacement and traction are prescribed, respectively. n_i is the unit normal vector outwards on S. The plastic strain ϵ^p_{ij} and thermal strain ϵ^θ_{ij} are included in the stress-strain relation, eq. (2.1.3), where T denotes temperature and $\Delta\epsilon^{ep}_{ij}$ is defined by the sum of the incremental elastic strain $\Delta\epsilon^e_{ij}$ and the incremental plastic strain $\Delta\epsilon^p_{ij}$ as

$$\Delta\epsilon^{ep}_{ij} = \Delta\epsilon^e_{ij} + \Delta\epsilon^p_{ij} \qquad (2.1.7)$$

For the thermal elastic-plastic problem, the incremental strain $\Delta\epsilon_{ij}$ can be decomposed as follows:

$$\Delta\epsilon_{ij} = \Delta\epsilon^e_{ij} + \Delta\epsilon^p_{ij} + \Delta\epsilon^\theta_{ij} = \Delta\epsilon^{ep}_{ij} + \Delta\epsilon^\theta_{ij} \qquad (2.1.8)$$

$E^{ep}_{ijk\ell}$ and G^{ep}_{ij} in eq. (2.1.3) are given as follows:

$$E^{ep}_{ijk\ell} = E^e_{ijk\ell} - \cfrac{E^e_{ijmn}\,\dfrac{\partial f}{\partial\sigma_{mn}}\,\dfrac{\partial f}{\partial\sigma_{op}}E^e_{opk\ell}}{-\dfrac{\partial f}{\partial\epsilon^p_{mn}}\dfrac{\partial f}{\partial\sigma_{mn}} + \dfrac{\partial f}{\partial\sigma_{mn}}E^e_{mnop}\dfrac{\partial f}{\partial\sigma_{op}}} \qquad (2.1.9)$$

$$G^{ep}_{ij} = \frac{\partial E^e_{ijk\ell}}{\partial T}\epsilon^e_{k\ell} - \cfrac{E^e_{ijk\ell}\,\dfrac{\partial f}{\partial\sigma_{k\ell}}\left(\dfrac{\partial f}{\partial\sigma_{mn}}\dfrac{\partial E^e_{mnop}}{\partial T}\epsilon^e_{op} + \dfrac{\partial f}{\partial T}\right)}{-\dfrac{\partial f}{\partial\epsilon^p_{mn}}\dfrac{\partial f}{\partial\sigma_{mn}} + \dfrac{\partial f}{\partial\sigma_{mn}}E^e_{mnop}\dfrac{\partial f}{\partial\sigma_{op}}} \qquad (2.1.10)$$

in which $E^e_{ijk\ell}$ and f denote the elastic modulus tensor and the yield function, respectively. The
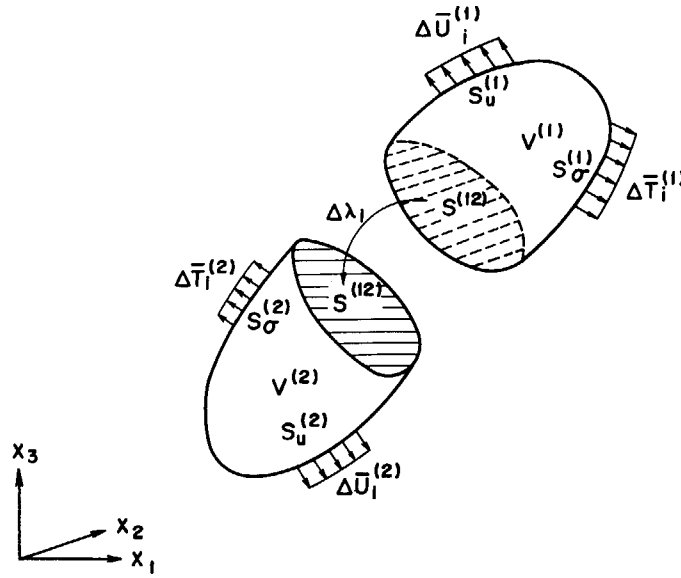
Fig. 2.1.1 Continuum divided into two parts.

derivation of eqs. (2.1.9) and (2.1.10) is referred to Appendix A. In the report, the usual summation convention for repeated indices is used with a comma followed by i indicating the differentiation with respect to x_i.

Next, let us consider the domain shown in **Fig. 2.1.1**, where the body V is tentatively split into two parts $V^{(1)}$ and $V^{(2)}$ which are assumed to be contiguous on $S^{(12)}$. In this case, eqs. (2.1.1)–(2.1.5) should be established in both bodys $V^{(1)}$ and $V^{(2)}$ as follows:

$$\Delta\sigma_{ij,j}^{(\alpha)} + \Delta\bar{P}_i^{(\alpha)} = 0 \qquad\qquad \text{(in } V^{(\alpha)}) \qquad\qquad (2.1.11)$$

$$\Delta\epsilon_{ij}^{(\alpha)} = \frac{1}{2}(\Delta u_{i,j}^{(\alpha)} + \Delta u_{j,i}^{(\alpha)}) \qquad \text{(in } V^{(\alpha)}) \qquad\qquad (2.1.12)$$

$$\Delta\sigma_{ij}^{(\alpha)} = (E_{ijk\ell}^{ep})^{(\alpha)}(\Delta\epsilon_{k\ell}^{ep})^{(\alpha)} + (G_{ij}^{ep})^{(\alpha)}\Delta T^{(\alpha)} \qquad \text{(in } V^{(\alpha)}) \qquad (2.1.13)$$

$$\Delta u_i^{(\alpha)} = \Delta\bar{u}_i^{(\alpha)} \qquad\qquad \text{(on } S_u^{(\alpha)}) \qquad\qquad (2.1.14)$$

$$\Delta T_i^{(\alpha)} = \Delta\bar{T}_i^{(\alpha)} \qquad\qquad \text{(on } S_\sigma^{(\alpha)}) \qquad\qquad (2.1.15)$$

Here, $(\ )^{(\alpha)}$ denotes the variable belonging to the fictitious region α, $\alpha = 1$ and 2. The continuity of the two parts of the body $V^{(1)}$ and $V^{(2)}$ is assured by the following equations:

$$\Delta u_i^{(1)} = \Delta u_i^{(2)} \qquad\qquad \text{(on } S^{(12)}) \qquad\qquad (2.1.16)$$

$$\Delta T_i^{(1)} + \Delta T_i^{(2)} = 0 \qquad\qquad \text{(on } S^{(12)}) \qquad\qquad (2.1.17)$$

The modified principle of virtual work which provides eqs. (2.1.11), (2.1.15)–(2.1.17) as the Euler equations is given as follows:[12]

$$\sum_{\alpha=1}^{2}\left[\int_{V^{(\alpha)}}\Delta\sigma_{ij}^{(\alpha)}\,\delta(\Delta\epsilon_{ij}^{(\alpha)})dV - \int_{V^{(\alpha)}}\Delta\bar{P}_i^{(\alpha)}\,\delta(\Delta u_i^{(\alpha)})dV\right.$$

$$\left. - \int_{S_\sigma^{(\alpha)}}\Delta\bar{T}_i^{(\alpha)}\,\delta(\Delta u_i^{(\alpha)})dS\right] - \int_{S^{(12)}}\delta\left[\Delta\lambda_i(\Delta u_i^{(1)} - \Delta u_i^{(2)})\right]dS$$

$$= 0 \qquad\qquad\qquad\qquad (2.1.18)$$

where δ denotes the virtual variation. $\Delta\lambda_i$ in the above equation are the Lagrange multipliers and physically equivalent to the traction forces on $S^{(12)}$, ΔT_i. The continuity condition of the displacement on $S^{(12)}$ i.e. eq. (2.1.16), is taken into account in the last term of the left hand side of eq. (2.1.18).

2.1.2 Finite Element Formulation

The use of different kinds of elements may be effective in the analysis of the local behavior of a complex structure. In this case, the continuity condition of displacement is often violated at the boundary of different kinds of elements. Thus, the modified principle of virtual work given in eq. (2.1.18) is used to formulate the finite element equilibrium equation.

The displacements in $V^{(\alpha)}$, $\alpha = 1$ and 2, and on $S^{(12)}$ can be written in terms of nodal displacements $\Delta q_j{}^{(\alpha)}$, $\alpha = 1$ and 2, as follows:

$$\Delta u_i{}^{(\alpha)} = \phi_{ij}^{(\alpha)} \Delta q_j{}^{(\alpha)} \qquad \text{(in } V^{(\alpha)}\text{)} \qquad (2.1.19)$$

$$\Delta u_i{}^{(\alpha)} = \psi_{ij}^{(\alpha)} \Delta q_j{}^{(\alpha)} \qquad \text{(on } S^{(12)}\text{)} \qquad (2.1.20)$$

in which $\phi_{ij}^{(\alpha)}$, $\alpha = 1$ and 2, are the interpolation functions in the body $V^{(\alpha)}$, while $\psi_{ij}^{(\alpha)}$, $\alpha = 1$ and 2, are the interpolation function of the connection elements between the body $V^{(1)}$ and $V^{(2)}$. The Lagrange multipliers $\Delta\lambda_i$ are also interpolated as follows:

$$\Delta\lambda_i = \Omega_{ij}\Delta r_j \qquad (2.1.21)$$

where Ω_{ij} and Δr_j represent the interpolation functions defined on $S^{(12)}$ and the generalized coordinates, respectively. Using eqs. (2.1.12), (2.1.13) and (2.1.19), the strain-displacement and stress-strain relations are written in the following form:

$$\Delta\epsilon_{ij}^{(\alpha)} = B_{ijk}^{(\alpha)} \Delta q_k{}^{(\alpha)} \qquad \text{(in } V^{(\alpha)}\text{)} \qquad (2.1.22)$$

$$\Delta\sigma_{ij}^{(\alpha)} = (E_{ijk\ell}^{ep})^{(\alpha)} \{ B_{k\ell m}^{(\alpha)} \Delta q_m^{(\alpha)} - (\Delta\epsilon_{k\ell}^{\theta})^{(\alpha)} \} + G_{ij}^{(\alpha)} \Delta T^{(\alpha)}$$

$$\text{(in } V^{(\alpha)}\text{)} \qquad (2.1.23)$$

in which

$$B_{ijk}^{(\alpha)} = \frac{1}{2} (\phi_{ik,j}^{(\alpha)} + \phi_{jk,i}^{(\alpha)}) \qquad (2.1.24)$$

Introducing eqs. (2.1.19)–(2.1.23) into eq. (2.1.18) leads to the following equations:

$$\sum_{\alpha=1}^{2} \delta (\Delta q_i{}^{(\alpha)}) (K_{ij}^{(\alpha)}\Delta q_j{}^{(\alpha)} + \hat{K}_{ij}^{(\alpha)}\Delta r_j{}^{(\alpha)} - \Delta F_i{}^{(\alpha)})$$

$$+ \sum_{\alpha=1}^{2} \delta (\Delta r_i) \hat{K}_{ij}^{(\alpha)}\Delta q_j{}^{(\alpha)} = 0 \qquad (2.1.25)$$

where

$$K_{ij}^{(\alpha)} = \int_{V^{(\alpha)}} (E_{mnk\ell}^{ep})^{(\alpha)} B_{mni} B_{k\ell j} dV \qquad (2.1.26)$$

$$\hat{K}_{ij}^{(\alpha)} = \text{sign} (\alpha) \int_{S^{(12)}} \psi_{ik}^{(\alpha)} \Omega_{kj} dS \qquad (2.1.27)$$

$$\Delta F_i^{(\alpha)} = \int_{V^{(\alpha)}} \phi_{ij}^{(\alpha)} \Delta\bar{P}_j^{(\alpha)} dV + \int_{S_\sigma^{(\alpha)}} \phi_{ij}^{(\alpha)} \Delta\bar{T}_j^{(\alpha)} dS$$

$$+ \int_{V^{(\alpha)}} (E_{ijk\ell}^{ep})^{(\alpha)} B_{jkm} (\Delta\epsilon_{m\ell}^{\theta})^{(\alpha)} dV$$

$$- \int_{V^{(\alpha)}} B_{ijk}^{(\alpha)} G_{jk}^{(\alpha)} \Delta T^{(\alpha)} dV \qquad (2.1.28)$$

The functions $sign$ (α), $\alpha = 1$ and 2, in eq. (2.1.27) are defined as follows:

$sign$ $(1) = -1$

$sign$ $(2) = 1$ (2.1.29)

Since $\delta(\Delta q_i^{(\alpha)})$, $\alpha = 1$ and 2, and $\delta(\Delta r_i)$ are arbitrary, the following equilibrium equation is obtained from eq. (2.1.25):

$$
\begin{bmatrix} K^{(1)} & 0 & \hat{K}^{(1)} \\ & K^{(2)} & \hat{K}^{(2)} \\ \text{sym.} & & 0 \end{bmatrix}
\begin{Bmatrix} \Delta q^{(1)} \\ \Delta q^{(2)} \\ \Delta r \end{Bmatrix}
=
\begin{Bmatrix} \Delta F^{(1)} \\ \Delta F^{(2)} \\ 0 \end{Bmatrix}
\qquad (2.1.30)
$$

$\hat{K}^{(1)}$ and $\hat{K}^{(2)}$ in the above equation represent the stiffness matrices relevant to the connection elements connecting different kinds of elements. The detailed forms of these matrices are given in the next section.

In the EPAS-J1 program, the equilibrium equation (2.1.30) is solved using the wave front method.

2.2 Connection Element

The EPAS-J1 program has various kinds of elements which are briefly described in Appendix B. More detailed description of most of the elements included in the EPAS-J1 program is given in the standard text books on the finite element method such as ref. (13). Therefore, only the formulation of the connection elements is shown in this report. The notations used in this section are the same as those in the previous section.

2.2.1 Connection Element between Flat Shell Element and Beam Element
— BOUND3

The connection element (BOUND3), which is conceptually a triangular shape as shown in **Fig. 2.2.1**, connects the three-dimensional beam element (BEAM3D) to the 4-node flat shell element (FSHEL4). Provided that the three-dimensional beam and shell elements, respectively, correspond to $\alpha = 1$ and 2, and $S_e^{(12)}$ represents the area occupied by one of the connection elements, $\{\Delta u^{(\alpha)}\}$ and $\{\Delta q^{(\alpha)}\}$, $\alpha = 1$ and 2, in eq. (2.1.20) can be written as follows:
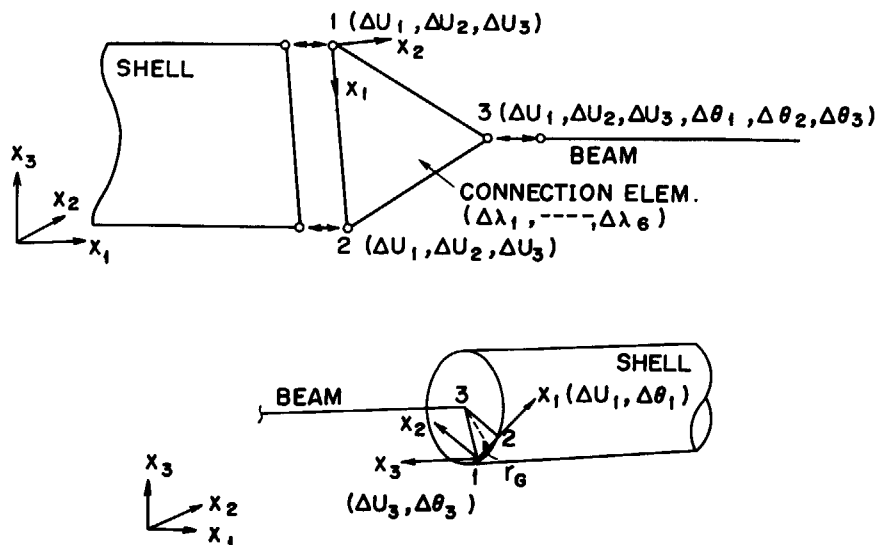

Fig. 2.2.1 Conception of connection element between flat shell and beam elements — BOUND3.

$$\{\Delta u^{(1)}\} = \{\Delta u^{(2)}\} = \Delta \{ u_1, u_2, u_3, \theta_1, \theta_2, \theta_3 \}^t \qquad (\text{on } S_e^{(12)}) \qquad (2.2.1)$$

$$\{\Delta q^{(1)}\} = \Delta \{ u_1^3, u_2^3, u_3^3, \theta_1^3, \theta_2^3, \theta_3^3 \}^t \qquad (\text{on } S_e^{(12)}) \qquad (2.2.2a)$$

$$\{\Delta q^{(2)}\} = \Delta \{ u_1^1, u_2^1, u_3^1, u_1^2, u_2^2, u_3^2 \}^t \qquad (\text{on } S_e^{(12)}) \qquad (2.2.2b)$$

in which u and θ represent the translational and rotational components of displacement, respectively, and the superscripts and the subscripts on u and θ denote the nodal numbers and the coordinate, respectively. Considering for example the connection between a beam and a cylindrical shell as shown in **Fig. 2.2.1**, the interporation functions $[\psi^{(\alpha)}]$, $\alpha = 1$ and 2, can be written as follows:

$$[\psi^{(1)}] = \begin{bmatrix} 1 & 0 & 0 & 0 & 0 & 0 \\ 0 & 1 & 0 & 0 & 0 & 0 \\ 0 & 0 & 1 & 0 & 0 & 0 \\ 0 & 0 & -1/r_G & 1 & 0 & 0 \\ 0 & 0 & 0 & 0 & 1 & 0 \\ 0 & 0 & 0 & 0 & 0 & 1 \end{bmatrix} \qquad (\text{on } S_e^{(12)}) \qquad (2.2.3a)$$

$$[\psi^{(2)}] = \begin{bmatrix} \hat{\psi}_1 & 0 & 0 & \hat{\psi}_2 & 0 & 0 \\ 0 & \hat{\psi}_1 & 0 & 0 & \hat{\psi}_2 & 0 \\ 0 & 0 & \hat{\psi}_1 & 0 & 0 & \hat{\psi}_2 \\ 0 & 0 & \hat{\psi}_1/r_G & 0 & 0 & -\hat{\psi}_2/r_G \\ 0 & 0 & 1/\ell & 0 & 0 & -1/\ell \\ 0 & -1/\ell & 0 & 0 & -1/\ell & 0 \end{bmatrix} \qquad (\text{on } S_e^{(12)}) \qquad (2.2.3b)$$

in which

$$\hat{\psi}_1 = 1 - \frac{x_1}{\ell}, \quad \hat{\psi}_2 = \frac{x_1}{\ell}, \quad \ell = | x_i^2 - x_i^1 |$$

$$r_G = | x_i^3 - x_i^G |, \quad x_i^G = \frac{1}{2}(x_i^1 + x_i^2) \qquad (2.2.4)$$

In eq. (2.2.4), $| \ |$ denotes the distance between two points. Assuming that the Langrange multipliers are constant in the connection element, $\{\Delta\lambda\}$, $\{\Delta r\}$ and $[\Omega]$ are given, respectively, as follows:

$$\{\Delta\lambda\} = \Delta \{\lambda_1, \lambda_2, \ldots\ldots, \lambda_6 \}^t \qquad (2.2.5a)$$

$$\{\Delta r\} = \Delta \{r_1, r_2, \ldots\ldots, r_6 \}^t \qquad (2.2.5b)$$

$$\{\Omega\} = [I] \qquad (2.2.6)$$

where $[I]$ in eq. (2.2.6) is a 6×6 unit matrix. Introducing eqs. (2.2.3a), (2.2.3b) and (2.2.6) into eq. (2.1.27) leads to the following equations:

$$[\hat{K}^{(1)}]_e = -\int_{S_e^{(12)}} [\psi^{(1)}]^t [\Omega] dS = -\int_0^\ell [\psi^{(1)}]^t d\hat{x} \qquad (2.2.7)$$

$$[\hat{K}^{(2)}]_e = \int_{S_e^{(12)}} [\psi^{(2)}]^t [\Omega] dS = \int_0^\ell [\psi^{(2)}]^t d\hat{x} \qquad (2.2.8)$$

Assemblage of the matrices given in eqs. (2.2.7) and (2.2.8) for all connection elements yields the connection matrices of complete structure $[\hat{K}^{(\alpha)}]$, $\alpha = 1$ and 2.

2.2.2 Connection Element between Solid Element and Flat Shell Element — BOUND8

The connection element (BOUND8), which is conceptually a triangular prism as shown in **Fig. 2.2.2**, connects the 4-node flat shell element (FSHEL4) to the 16-node element (SOLID16). Provided that the flat shell and solid elements, respectively, correspond to $\alpha = 1$ and 2, and $S_e^{(12)}$ represents the area occupied by one of the connection elements, $\{\Delta u^{(\alpha)}\}$ and $\{\Delta q^{(\alpha)}\}$, $\alpha = 1$ and 2, in eq. (2.1.20) can be written as follows:

$$\{\Delta u^{(1)}\} = \{\Delta u^{(2)}\} = \Delta\{ u_1, u_2, u_3, \theta_1, \theta_2, \theta_3 \}^t \tag{2.2.9}$$

$$\{\Delta q^{(1)}\} = \Delta\{ u_1^7, u_2^7, u_3^7, \theta_1^7, \theta_2^7, \theta_3^7, u_1^8, u_2^8, u_3^8, \theta_1^8, \theta_2^8, \theta_3^8 \}^t \tag{2.2.10a}$$

$$\{\Delta q^{(2)}\} = \Delta\{ u_1^1, u_2^1, u_3^1, u_1^2, u_2^2, u_3^2, \ldots\ldots, u_1^6, u_2^6, u_3^6 \}^t \tag{2.2.10b}$$

The displacements in the connection element are assumed to vary linearly along the side connected with the flat shell element. Then, the interpolation function $[\psi^{(1)}]$ is given as follows:

$$\{\Delta u^{(1)}\} = [\psi^{(1)}] \{\Delta q^{(1)}\} \qquad \text{(on } S_e^{(12)}) \tag{2.2.11}$$

$$[\psi^{(1)}] = [\phi_1^* [I] \ \phi_2^* [I]] \tag{2.2.12}$$

in which $[I]$ is a 6×6 unit matrix, and ϕ_1^* and ϕ_2^* are given as

$$\phi_1^* = \frac{1}{2}(1 - \xi), \phi_2^* = \frac{1}{2}(1 + \xi) \tag{2.2.13}$$

On the other hand, the translations in the plane of connection element connected with the solid element are represented using the shape function of the 6-node isoparametric element as follows:

$$\Delta u_j = \sum_{i=1}^{6} \hat{\phi}_i u_j^i \quad (j = 1, 2, 3) \qquad \text{(on } S_e^{(12)}) \tag{2.2.14}$$
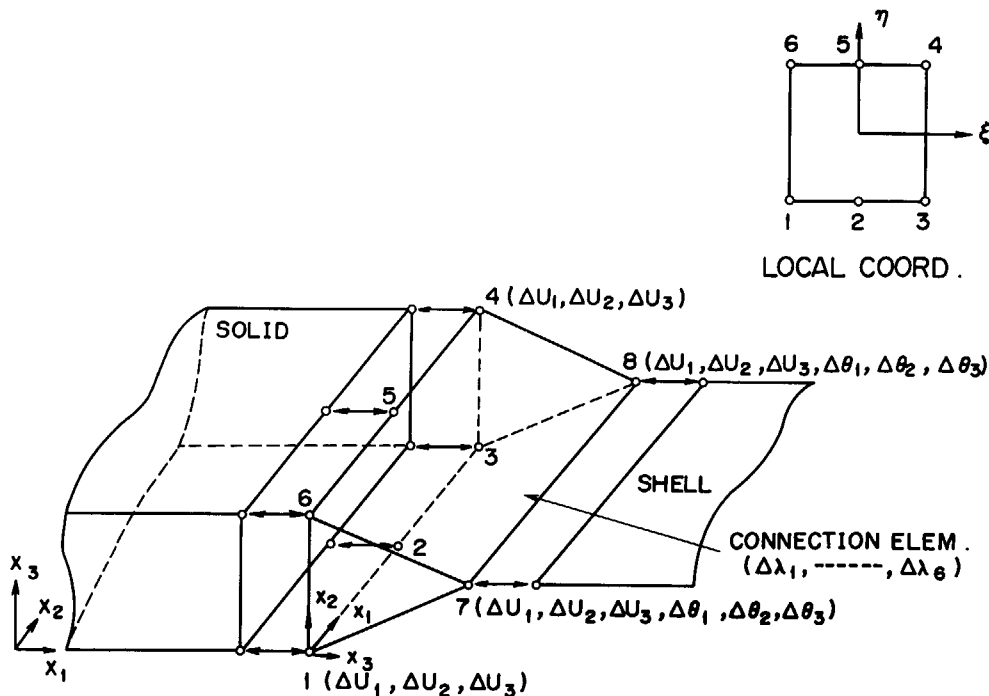

LOCAL COORD.

Fig. 2.2.2 Conception of connection element between solid and flat shell elements — BOUND8.

Using the above equation, the rotations can be written as follows:

$$\Delta\theta_1 = \frac{\partial\Delta u_3}{\partial x_2} = \sum_{i=1}^{6} \frac{\partial\hat{\phi}_i}{\partial x_2}\,\Delta u_3^i$$

$$\Delta\theta_2 = -\frac{\partial\Delta u_3}{\partial x_1} = -\sum_{i=1}^{6} \frac{\partial\hat{\phi}_i}{\partial x_1}\,\Delta u_3^i \qquad (2.2.15)$$

$$\Delta\theta_3 = \frac{1}{2}\left(\frac{\partial\Delta u_2}{\partial x_1} - \frac{\partial\Delta u_1}{\partial x_2}\right) = \frac{1}{2}\sum_{i=1}^{6}\left(\frac{\partial\hat{\phi}_i}{\partial x_1}\,\Delta u_2^i - \frac{\partial\hat{\phi}_i}{\partial x_2}\,\Delta u_1^i\right)$$

As shown in the above equations, out-of-plane rotations cannot be exactly expressed by the connection element. Since $\hat{\phi}_i$ are the functions of ξ and η, the derivatives of $\hat{\phi}_i$ with respect to the global coordinates are given as follows:

$$\left\{\begin{array}{c}\dfrac{\partial\hat{\phi}_i}{\partial x_1}\\[3mm]\dfrac{\partial\hat{\phi}_i}{\partial x_2}\end{array}\right\} = [J]^{-1}\left\{\begin{array}{c}\dfrac{\partial\hat{\phi}_i}{\partial\xi}\\[3mm]\dfrac{\partial\hat{\phi}_i}{\partial\eta}\end{array}\right\} \qquad (2.2.16)$$

$$[J]^{-1} = \begin{bmatrix} J'_{11} & J'_{12} \\[2mm] J'_{21} & J'_{22} \end{bmatrix} \qquad (2.2.17)$$

in which $[J]^{-1}$ is an inverse matrix of the Jacobian matrix. Substituting eq. (2.2.16) into eq. (2.2.15) yields:

$$\Delta\theta_1 = \sum_{i=1}^{6}\left(J'_{21}\frac{\partial\hat{\phi}_i}{\partial\xi} + J'_{22}\frac{\partial\hat{\phi}_i}{\partial\eta}\right)\Delta u_3^i$$

$$\Delta\theta_2 = -\sum_{i=1}^{6}\left(J'_{11}\frac{\partial\hat{\phi}_i}{\partial\xi} + J'_{12}\frac{\partial\hat{\phi}_i}{\partial\eta}\right)\Delta u_3^i \qquad (2.2.18)$$

$$\Delta\theta_3 = \frac{1}{2}\sum_{i=1}^{6}\left\{\left(J'_{11}\frac{\partial\hat{\phi}_i}{\partial\xi} + J'_{12}\frac{\partial\hat{\phi}_i}{\partial\eta}\right)\Delta u_2^i - \left(J'_{21}\frac{\partial\hat{\phi}_i}{\partial\xi} + J'_{22}\frac{\partial\hat{\phi}_i}{\partial\eta}\right)\Delta u_1^i\right\}$$

From eqs. (2.2.14) and (2.2.18), the interpolation function $[\psi^{(2)}]$ is given as follows:

$$\{\Delta u^{(2)}\} = [\psi^{(2)}]\,\{\Delta q^{(2)}\} \qquad (2.2.19)$$

$$[\psi^{(2)}] = \begin{bmatrix} \hat{\phi}_1 & 0 & 0 & \cdots & \hat{\phi}_6 & 0 & 0 \\ 0 & \hat{\phi}_1 & 0 & \cdots & 0 & \hat{\phi}_6 & 0 \\ 0 & 0 & \hat{\phi}_1 & \cdots & 0 & 0 & \hat{\phi}_6 \\ 0 & 0 & \alpha_1 & \cdots & 0 & 0 & \alpha_6 \\ 0 & 0 & -\beta_1 & \cdots & 0 & 0 & -\beta_6 \\ -\dfrac{\alpha_1}{2} & \dfrac{\beta_1}{2} & 0 & \cdots & -\dfrac{\alpha_6}{2} & \dfrac{\beta_6}{2} & 0 \end{bmatrix} \qquad (2.2.20)$$

in which

$$\alpha_i = J'_{21}\frac{\partial\hat{\phi}_i}{\partial\xi} + J'_{22}\frac{\partial\hat{\phi}_i}{\partial\eta}$$

$$\beta_i = J'_{11} \frac{\partial \hat{\phi}_i}{\partial \xi} + J'_{12} \frac{\partial \hat{\phi}_i}{\partial \eta}$$

Furthermore, using the nodal values $\Delta\lambda_i^7$ and $\Delta\lambda_i^8$ which have six degrees-of-freedom, respectively, the Langrange multipliers $\Delta\lambda_i$ are interpolated as:

$$\Delta\lambda_i = \hat{\psi}_1 \Delta\lambda_i^7 + \hat{\psi}_2 \Delta\lambda_i^8 \qquad (2.2.21)$$

If the Lagrange multipliers are assumed to be constant on the line between the nodes 7 and 8, the interpolation functions can be written as:

$$\hat{\psi}_1 = \hat{\psi}_2 = 1/2 \qquad (2.2.22)$$

On the other hand, when the Lagrange multipliers are assumed to vary lineary between the nodes 7 and 8, $\hat{\psi}_1$ and $\hat{\psi}_2$ become as follows:

$$\hat{\psi}_1 = \frac{1}{2}(1 - \xi), \quad \hat{\psi}_2 = \frac{1}{2}(1 + \xi) \qquad (2.2.23)$$

If $\{\Delta\lambda\}$ and $\{\Delta r\}$ are defined as

$$\{\Delta\lambda\} = \{\Delta\lambda_1, \Delta\lambda_2, \ldots, \Delta\lambda_6\}^t$$

$$\{\Delta r\} = \{\Delta\lambda_1^7, \ldots, \Delta\lambda_6^7, \Delta\lambda_1^8, \ldots, \Delta\lambda_6^8\}^t$$

$[\Omega]$ in eq. (2.1.22) can be written as

$$[\Omega] = \begin{bmatrix} \hat{\psi}_1 & & 0 & & \hat{\psi}_2 & & 0 \\ & \ddots & & & & \ddots & \\ 0 & & \hat{\psi}_1 & & 0 & & \hat{\psi}_2 \end{bmatrix} \qquad (2.2.24)$$

Substituting eqs. (2.2.12), (2.2.20) and (2.2.24) into eq. (2.1.27) and performing numerical integration lead to the connection matrices.

2.2.3 Connection Element between Solid Element and Flat Shell Element — BOUND10

The connection element BOUND10 shown in **Fig. 2.2.3** is used to connect the 4-node flat shell element to the 20-node solid element. The interpolation functions of the connection element and the Lagrange multipliers can be obtained in the same manner as BOUND8 element. Therefore, the detailed description of the connection element is omitted here.

2.3 Virtual Crack Extension Method Used to Determine Stress Intensity Factor

2.3.1 General Remarks

The virtual crack extension method[7)8)] is one of the methods used to determine the stress intensity factor. It is based on the energy method in which the energy release rate is calculated from the difference of the total potential energies of the two cracked structures whose crack lengths are slightly different. In the conventional energy method[14)], analyses are required twice to obtain the energy release rate, whereas in the virtual crack extension method analysis is required only one to obtain the energy release rate. It can be easily incorporated into an existing finite element program and provides comparatively accurate results. Therefore, EPAS-J1 program employs the virtual crack extension method to obtain the stress intensity factors. A detailed explanation of the method is presented in this section.
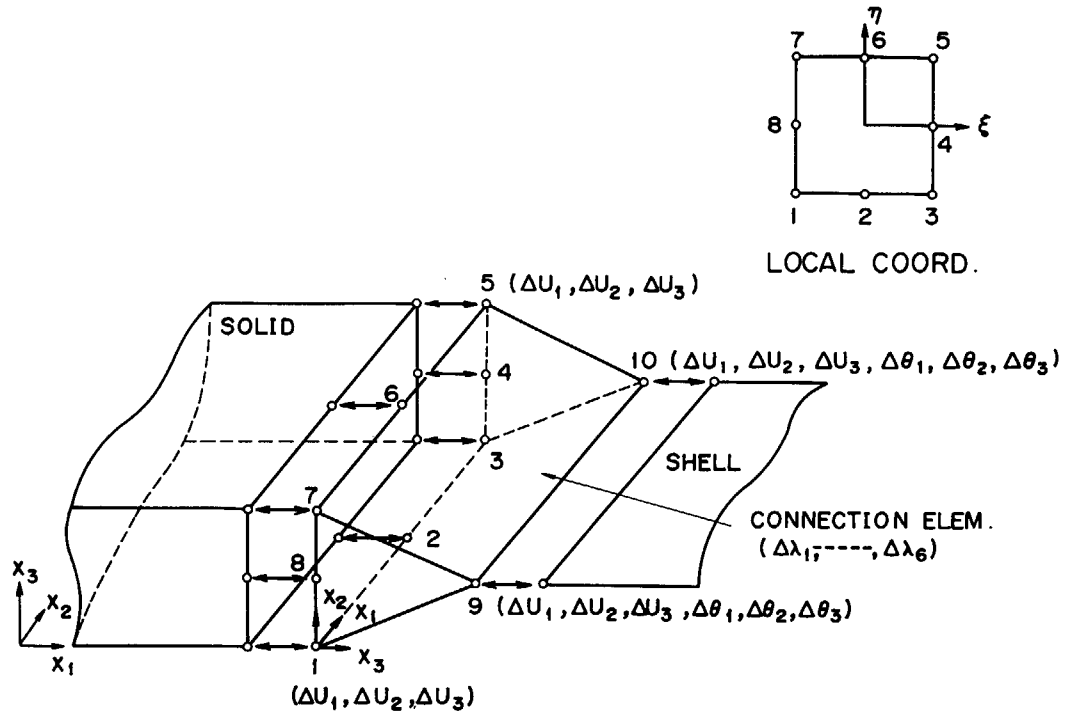
Fig. 2.2.3 Conception of connection element between solid and flat shell elements —
BOUND10.

The total potential energy can be written as follows, considering the effect of the thermal strain:

$$\pi = \frac{1}{2}\{u\}^t\,[K]\,\{u\} - \{u\}^t\,\{P\} - \{u\}^t\,\{P^\theta\}$$

(2.3.1)

where $[K]$ is the stiffness matrix, $\{u\}$ is the nodal displacement vector, and $\{P\}$ and $\{P^\theta\}$ are the nodal force vectors due to the external load and the thermal strain, respectively. Considering the small crack extension, the variation of the total potential energy due to the increase of crack surface A can be represented as follows:

$$\frac{\partial \pi}{\partial A} = \left\{\frac{\partial u}{\partial A}\right\}(\,[K]\,\{u\} - \{P\} - \{P^\theta\}\,) + \frac{1}{2}\{u\}^t\left[\frac{\partial K}{\partial A}\right]\{u\}$$

$$- \{u\}^t\left\{\frac{\partial P}{\partial A}\right\} - \{u\}^t\left\{\frac{\partial P^\theta}{\partial A}\right\}$$

$$= \frac{1}{2}\{u\}^t\left[\frac{\partial K}{\partial A}\right]\{u\} - \{u\}^t\left(\left\{\frac{\partial P}{\partial A}\right\} + \left\{\frac{\partial P^\theta}{\partial A}\right\}\right)$$

(2.3.2)

If no thermal strain, no body force and no crack surface force are assumed, eq. (2.3.2) can be simplified as follows:

$$\frac{\partial \pi}{\partial A} = \frac{1}{2}\{u\}^t\left[\frac{\partial K}{\partial A}\right]\{u\}$$

(2.3.3)

The stress intensity factor K is related to the energy release rate G as follows:

$$G \equiv -\left.\frac{\partial \pi}{\partial A}\right|_{load} = \frac{1 - \nu^2}{E}(K_I^2 + K_{II}^2) + \frac{1 + \nu}{E}K_{III}^2 \quad : \text{Plane Strain}$$

$$= \frac{1}{E}(K_I^2 + K_{II}^2 + K_{III}^2) \qquad\qquad : \text{Plane Stress}$$

(2.3.4)

where E and ν are, respectively, the modulus of elasticity and Poission's ratio, and K_I, K_{II} and K_{III} denote the stress intensity factors corresponding to mode I, II and III, respectively. The stress intensity factor for the single mode can be obtained from eq. (2.3.4), if the value of $\partial\pi/\partial A$ is known.

In the remainder of this section, the virtual crack extension methods are shown for the two- and three-dimensional crack problems.

2.3.2 Two-dimensional Crack Problem[7]

Now consider the virtual crack extension of the two-dimensional crack shown in **Fig. 2.3.1(a)**. In the figure Γ_1 is fixed and the x-coordinates of all nodes on and within an interior contour Γ_2 which surrounds the crack tip are incremented by the amount of $\Delta\ell$. The stiffness matrices of the elements inside an interior contour Γ_0 and outside an exterior contour Γ_1 remain unchanged during the virtual extension of the crack. Then, the first term of eq. (2.3.2) becomes

$$\frac{1}{2}\{u\}^t\left[\frac{\partial K}{\partial A}\right]\{u\} = \frac{1}{2}\sum_{i=1}^{n}\{u_i\}^t\left[\frac{\partial \hat{K}_i}{\partial A}\right]\{u_i\} \tag{2.3.5}$$

where $[\hat{K}_i]$ and $\{u_i\}$, $i = 1\sim n$, are the stiffness materices of the elements surrounded between two contours Γ_0 and Γ_1, the number of which is n, and the nodal displacement vectors corresponding to the stiffness matrices $[\hat{K}_i]$. Assuming the thickness to be t, the derivative of the stiffness matrix in eq. (2.3.5) can be written as follows:

$$\left[\frac{\partial \hat{K}_i}{\partial A}\right] = \frac{1}{\Delta\ell \cdot t}(\ [\hat{K}_i]_{\ell+\Delta\ell} - [\hat{K}_i]_\ell) \tag{2.3.6}$$

The second and third terms of eq. (2.3.2) can be also written as follows:

$$\{u\}^t\left(\left\{\frac{\partial P}{\partial A}\right\} + \left\{\frac{\partial P^\theta}{\partial A}\right\}\right) = \sum_{i=1}^{n}\{u_i\}^t\frac{\partial}{\partial A}(\ \{\hat{P}_i\} + \{\hat{P}_i^\theta\}\ ) \tag{2.3.7}$$

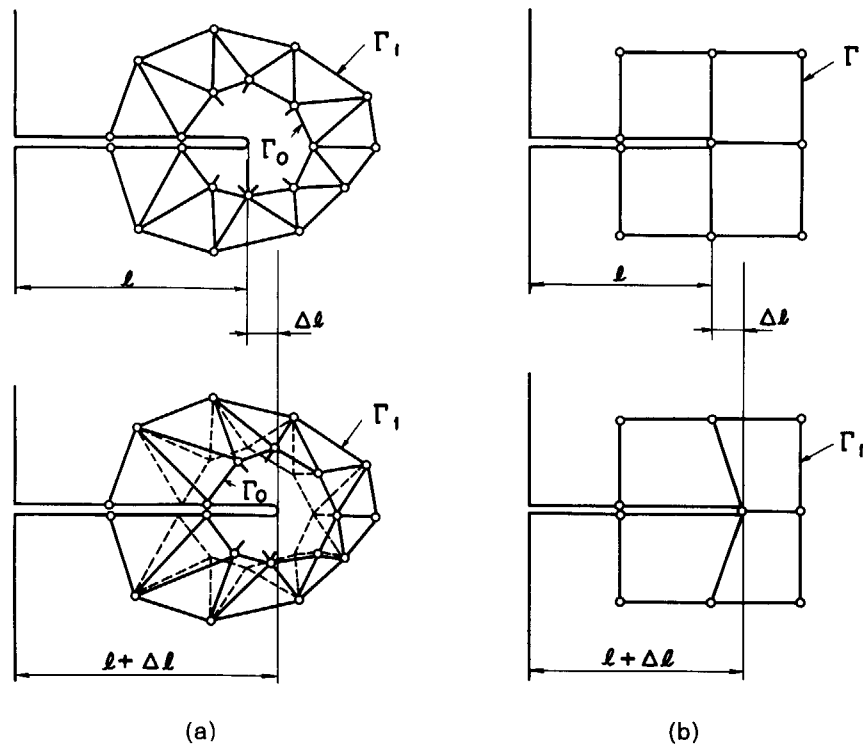(a)   (b)

Fig. 2.3.1 Virtual crack extension method for two dimensional crack.

in which $\{\hat{P}_i\}$ and $\{\hat{P}_i^\theta\}$, $i = 1\sim n$, denote, respectively, the nodal force vectors of the elements surrounded between two contours Γ_0 and Γ_1 due to the external force and the thermal strain. The derivative of the nodal force vectors in eq. (2.3.7) is given as follows:

$$\frac{\partial}{\partial A}(\{\hat{P}_i\} + \{\hat{P}_i^\theta\}) = \frac{1}{\Delta \ell \cdot t} \Delta(\{\hat{P}_i\} + \{\hat{P}_i^\theta\})$$

$$= \frac{1}{\Delta \ell \cdot t}(\{P_i^*\}_{\ell + \Delta \ell} - \{P_i^*\}_\ell) \tag{2.3.8}$$

in which

$$\{P_i^*\} = \{\hat{P}_i\} + \{\hat{P}_i^\theta\}$$

Substituting eqs. (2.3.5) and (2.3.7) into eq. (2.3.2), the energy release rate G can be written as:

$$G = -\frac{1}{2}\sum_{i=1}^n \{u_i\}^t \left[\frac{\partial \hat{K}_i}{\partial A}\right] \{u_i\} + \sum_{i=1}^n \{u_i\}^t \frac{\partial}{\partial A}(\{\hat{P}_i\} + \{\hat{P}_i^\theta\}) \tag{2.3.9}$$

Then, the stress intensity factors for the single mode can be obtained from eq. (2.3.4). As shown in **Fig. 2.3.1(b)**, the contour Γ_0 can be taken at the crack tip. In this case, eq. (2.3.9) can be used to calculate the energy release rate G by regarding n as the number of the elements, in the nodes of which crack tip is contained.

2.3.3 Three-demensional Crack Problem

The distribution of the stress intensity factor along a crack front is primarily important in the three-dimensional crack. Here is shown the method for calculating the energy release rate of the node allocated along the crack front.[1]

The variation of the potential energy $\Delta\pi$ can be written as follows, using the energy release rate $G(s)$ and the crack extension value $\Delta y(s)$ normal to the crack front.

$$\int_{\substack{\text{crack}\\\text{front}}} G(s)\,\Delta\ell(s)ds = -\Delta\pi \tag{2.3.10}$$

in which s denotes the coordinate taken on the crack front. A detailed discussion is given below for the two cases, where the sides of the elements on the crack front have linear and quardratic variations with s.

(I)   Linear Variation

The sides of the elements on the crack front vary linearly with s, when the 16-node solid elements (SOLID16) are allocated along the crack front. Let us consider an arbitrary side of the element on the crack front (12) as shown in **Fig. 2.3.2(a)** in which the x-axis corresponds to the side 12 and the y-axis is normal to the x-axis at the point 1. Assuming that the length of the side 12 is b and the coordinates of the points 1 and 2 are, respectively, -1 and 1 by the generalized coordinate ξ, the relation between x and ξ is given as follows:

$$x = \frac{1}{2}b(1 + \xi) \tag{2.3.11}$$

Then, the virtual extension value on the side Δy can be interpolated linearly by those of the points 1 and 2, i.e. Δy_1 and Δy_2, as follows:

$$\Delta y = \lfloor N_1 \ N_2 \rfloor \begin{Bmatrix} \Delta y_1 \\ \Delta y_2 \end{Bmatrix} \tag{2.3.12}$$

$$N_1 = \frac{1}{2}(1 - \xi), \quad N_2 = \frac{1}{2}(1 + \xi)$$

The energy release rate G can be also interpolated as the same manner above.

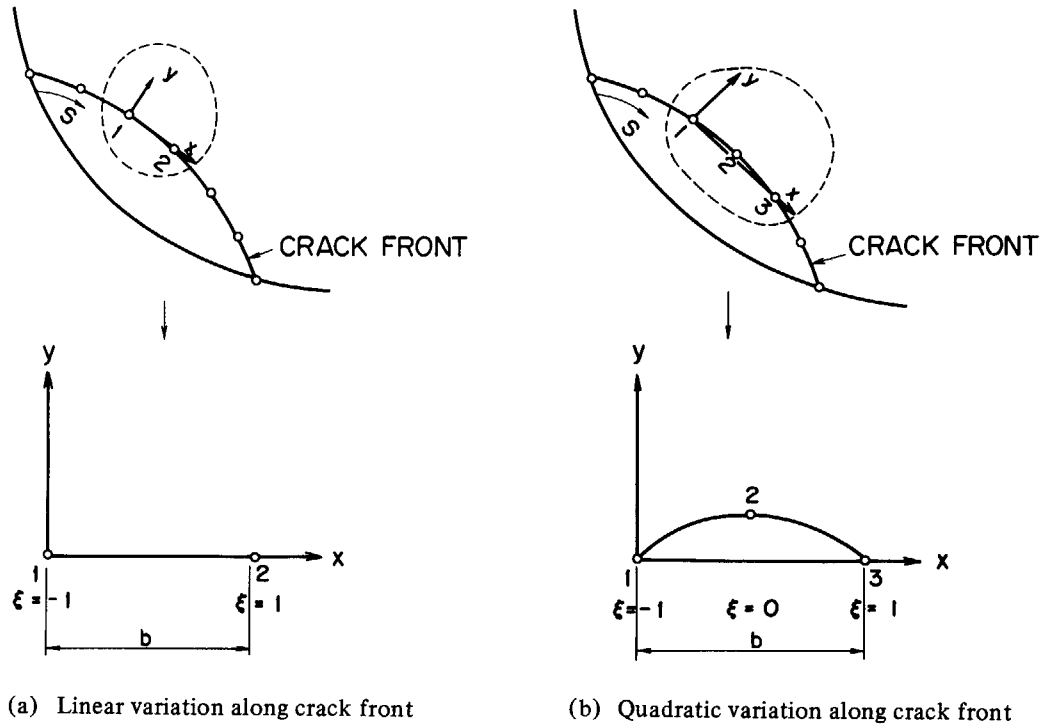(a) Linear variation along crack front   (b) Quadratic variation along crack front

Fig. 2.3.2 Virtual crack extension method for three diemnsional crack.

$$G = \lfloor N_1 \quad N_2 \rfloor \begin{Bmatrix} G_1 \\ G_2 \end{Bmatrix} \tag{2.3.13}$$

in which G_1 and G_2 denote the energy release rates at the points 1 and 2, respectively. Substituting eqs. (2.3.12) and (2.3.13) into eq. (2.3.10) yields the following equation.

$$\Delta\pi = -\int_s G(s)\,\Delta\ell(s)ds = -\int_s G(s)\,\Delta y ds$$

$$= -\lfloor \Delta y_1 \quad \Delta y_2 \rfloor \int_s \begin{bmatrix} N_1^2 & N_1 N_2 \\ N_1 N_2 & N_2^2 \end{bmatrix} ds \begin{Bmatrix} G_1 \\ G_2 \end{Bmatrix}$$

$$= \lfloor \Delta y_1 \quad \Delta y_2 \rfloor \,[\hat{F}_2]\, \begin{Bmatrix} G_1 \\ G_2 \end{Bmatrix} \tag{2.3.14}$$

The matrix $[\hat{F}_2]$ is given as follows:

$$[\hat{F}_2] = -\int_s \begin{bmatrix} N_1^2 & N_1 N_2 \\ N_1 N_2 & N_2^2 \end{bmatrix} ds = -\int_{-1}^{1} \frac{b}{2} \begin{bmatrix} N_1^2 & N_1 N_2 \\ N_1 N_2 & N_2^2 \end{bmatrix} d\xi$$

$$= -\frac{b}{2} \begin{bmatrix} 2 & 1 \\ 1 & 2 \end{bmatrix} \tag{2.3.15}$$

where the following equation is used.

$$ds \approx dx = \frac{b}{2}d\xi$$

From eqs. (2.3.14) and (2.3.15), $\Delta\pi$ becomes as follows:

$$\Delta\pi = -\frac{b}{6}\{(2G_1 + G_2)\Delta y_1 \quad + 2G_2)\Delta y_2\} \tag{2.3.16}$$

Finally, the following matrix form equation is obtained from eq. (2.3.16).

$$\left\{ \begin{array}{c} \dfrac{\Delta\pi_1}{\Delta y_1} \\[2mm] \dfrac{\Delta\pi_2}{\Delta y_2} \end{array} \right\} = [\hat{F}_2] \left\{ \begin{array}{c} G_1 \\ G_2 \end{array} \right\} \tag{2.3.17}$$

Assemblage of the above equation for all sides of elements on the crack front yields the equation for calculating the energy release rate at the nodes on the crack front as follows:

$$[F_2]\{G\} = \left\{ \dfrac{\partial\pi}{\partial y} \right\} \tag{2.3.18}$$

(II) Quadratic Variation

The sides of the elements on the crack front have quadratic variation with s, when the 20-node solid elements (SOLID20) are allocated along the crack front. Let us consider an arbitrary side of the element on the crack front (123) as shown in **Fig. 2.3.2(b)** in which the x-axis corresponds to the side 13 and the y-axis is normal to the x-axis at the point 1. Assuming that the length of the side 13 is b and the coordinates of the points 1, 2 and 3 are, respectively, -1, 0 and 1 by the generalized coordinate ξ, the relation between x and ξ is given as follows.

$$x = \frac{1}{2} b\xi (1 + \xi) \tag{2.3.19}$$

Then, the virtual extension value on the side Δy can be interpolated using quadratic polynomials by those of the points 1, 2 and 3, i.e. Δy_1, Δy_2 and Δy_3, as follows:

$$\Delta y = \lfloor N_1 \ N_2 \ N_3 \rfloor \left\{ \begin{array}{c} \Delta y_1 \\ \Delta y_2 \\ \Delta y_3 \end{array} \right\} \tag{2.3.20}$$

$$N_1 = \frac{1}{2}\xi(\xi - 1), \quad N_2 = 1 - \xi^2, \quad N_3 = \frac{1}{2}\xi(\xi + 1)$$

The energy release rate G can be also interpolated as the same manner above.

$$G = \lfloor N_1 \ N_2 \ N_3 \rfloor \left\{ \begin{array}{c} G_1 \\ G_2 \\ G_3 \end{array} \right\} \tag{2.3.21}$$

in which G_1, G_2 and G_3 denote the energy release rates at the points 1, 2 and 3, respectively. The following matrix form equation is obtained by the same procedure presented in (I).

$$\left\{ \begin{array}{c} \dfrac{\Delta\pi_1}{\Delta y_1} \\[2mm] \dfrac{\Delta\pi_2}{\Delta y_2} \\[2mm] \dfrac{\Delta\pi_3}{\Delta y_3} \end{array} \right\} = [\hat{F}_3] \left\{ \begin{array}{c} G_1 \\ G_2 \\ G_3 \end{array} \right\} \tag{2.3.22}$$

in which

$$[\hat{F}_3] = -\frac{b}{30} \begin{bmatrix} 4 & 2 & -1 \\ 2 & 16 & 2 \\ -1 & 2 & 4 \end{bmatrix} \tag{2.3.23}$$

Assemblage of the above equation for all sides of the elements on the crack front leads to the equation for calculating energy release rate at the nodes on the crack front as follows:

$$[F_3] \{G\} = \left\{ \frac{\partial \pi}{\partial y} \right\}$$

(2.3.24)

The energy release rate at the nodes on the crack front can be obtained from eqs. (2.3.18) or (2.3.24), because the right hand side of these equation is a known value calculated from virtual crack etension. Furthermore, the stress intensity factors of mode I along the crack front can be obtained from eq. (2.3.4) as follows, by assuming the plane strain condition.

$$K_I = \sqrt{\frac{G}{1 - \nu^2}}$$

(2.3.25)

The stress intensity factors K_I, K_{II} and K_{III} for the mixed mode cannot be dealt with by the method presented above, because according to eq. (2.3.4) these stress intensity factors cannot be obtained in the separate form, even if energy release rate G is a known value. Then, a new virtual crack extension method is proposed in Appendix C to obtain the stress intensity factors for the mixed mode two-dimensional crack problem.

3. Numerical Examples and Discussion

Some numerical examples analyzed by the EPAS-J1 program and discussion on the results are presented in this chapter. Namely, the accuracy of the connection elements employed in the EPAS-J1 program is confirmed in Section 3.1. In Section 3.2, relatively simple problems of the two- and three-dimensional cracks are analyzed to show the effectiveness of the virtual crack extension method. In Section 3.3, the stress intensity factors are obtained using the connection element.

3.1 Numerical Tests on Connection Elements

The problem presented in ref. (15) was taken to confirm the accuracies of the connection elements employed in the EPAS-J1 program and the results were compared with those of other methods.

Figure 3.1.1 shows the analytical model composed of solid and plate parts, the dimensions of which are given in the same figure. In this structure, the origin of the coordinate system is completely fixed. The modulus of elastisity and Poission's ratio were assumed to be 2.0×10^4 kg/mm^2 and 0.3, respectively. The six loading conditions shown in **Fig. 3.1.2** were considered in the analysis. The following six cases of analyses were performed by the EPAS-J1 program.

CASE 1: The structure was modeled by SOLID16, BOUND8 and FSHEL4 elements. All SOLID16 elements in the connection plane are connected to FSHEL4 elements by BOUND8 elements, in which the Lagrange multiplier was assumed to be constant — Refer to **Fig. 3.1.3(a)**.

CASE 2: The same finite element modeling as in CASE 1 was used in the analysis but the Lagrange multiplier was assumed to vary linearly in the connection element BOUND8 — Refer to **Fig. 3.1.3(a)**.

CASE 3: The structure was modeled by SOLID20, BOUND10 and FSHEL4 elements. All SOLID20 elements in the connection plane are connected to FSHEL4

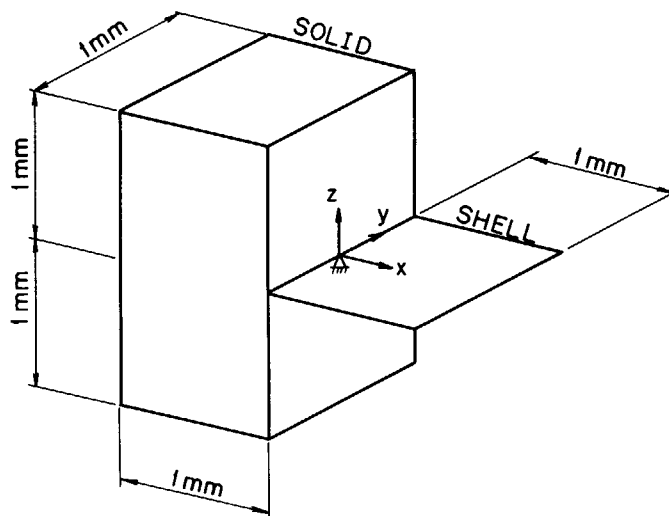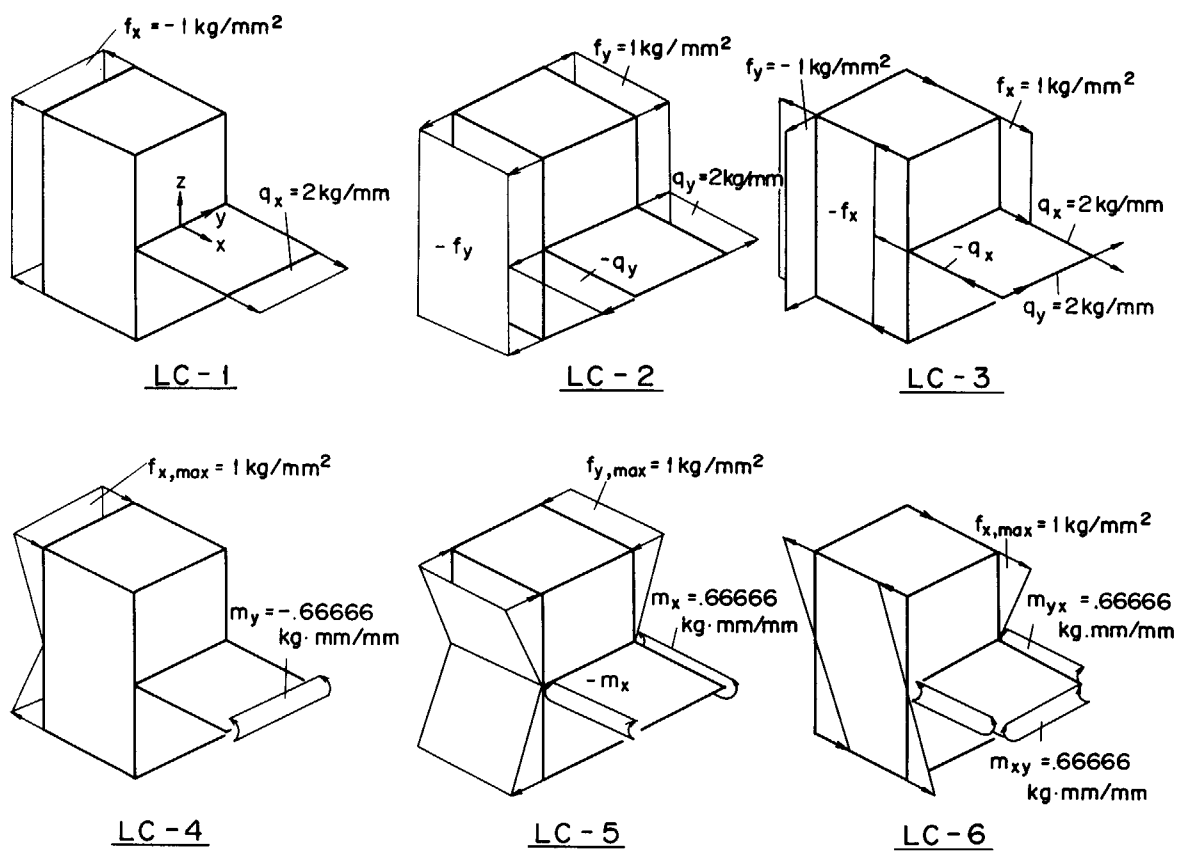**Fig. 3.1.1** Model composed of solid and plate.

Fig. 3.1.2 Loading conditions.

CASE 1 , CASE 2 , CASE 6   CASE 3, CASE 4 , CASE 5

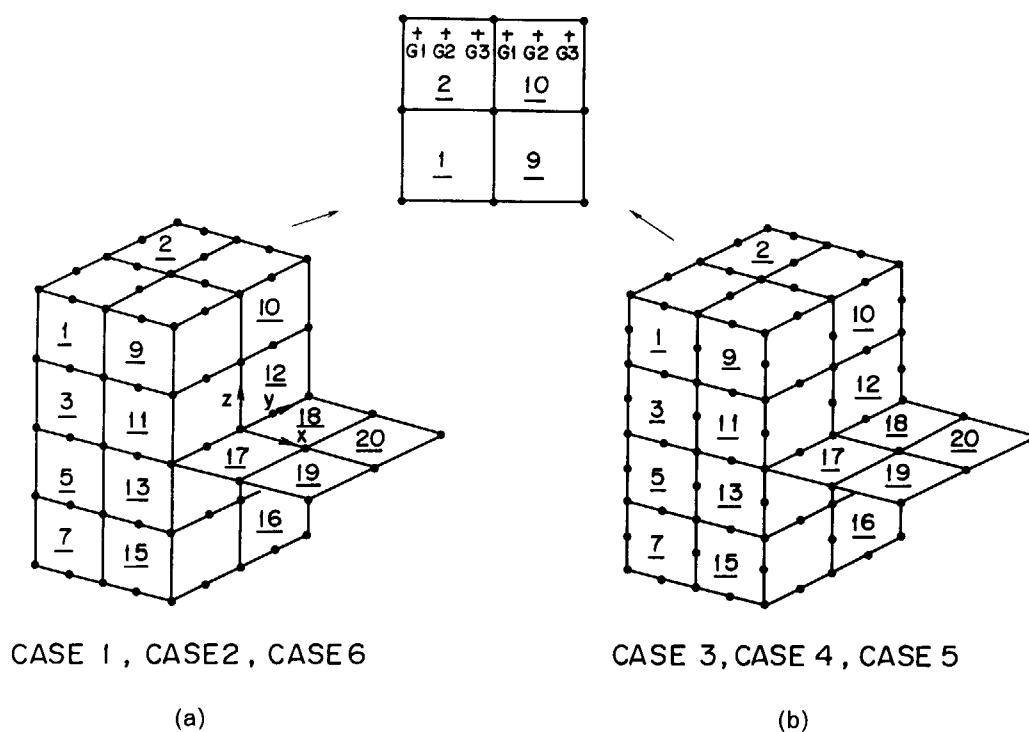(a)   (b)

Fig. 3.1.3 Finite element mesh of CASE 1-6.

elements by BOUND10 elements, in which the Lagrange multiplier was assumed to be constant — Refer to **Fig. 3.1.3(b)**.

CASE 4: The same finite element modeling as in CASE 3 was used in the analysis but the Lagrange multiplier was assumed to vary linearly in the connection element BOUND10 — Refer to **Fig. 3.1.3(b)**.

CASE 5: SOLID20, BOUND10 and FSHEL4 elements were used to model the structure. In this case, four couples of the elements (9, 11), (10, 12), (13, 15) and (14, 16) shown in **Fig. 3.1.3(a)** were connected to FSHEL4 elements by BOUND10 elements.

CASE 6: The structure was modeled by SOLID16 and FSHEL4 elements. A set of linear constraint equations was used to connect these two kinds of elements. Considering that the displacements of solid are subjected to those of shell and assuming that the rotation of shell are small, i.e., $\theta = \theta_x \approx \theta_y \approx \theta_z \approx 0$, the displacements of solid are related with those of shell as follows:

$$U_{solid} = U_{shell} + z\theta_y - y\theta_z \qquad (3.1)$$

$$V_{solid} = V_{shell} - z\theta_x \qquad (3.2)$$

$$W_{solid} = W_{shell} \qquad (3.3)$$

in which U, V and W are the displacements of x, y and z directions, respectively, and the subscripts of solid and shell denote the components of the solid and shell parts, respectively. Among the above equations, eq. (3.1) is applied to the all nodes in the connection plane, while eqs. (3.2) and (3.3) are applied to only the nodes on the intersectional line of the solid and shell parts.

Furthermore, the results were quoted from ref. (15). The method used in ref. (15) are described below.

CASE 7: The anisotropic shell element was used to connect solid element to shell element. **Figure 3.1.4** shows the finite element model for this case. The 8-node solid elements and the 4-node flat shell elements were used to model the solid and shell parts, respectively. The anisotropic element used as a connection element was assumed to have the following meterial properties:
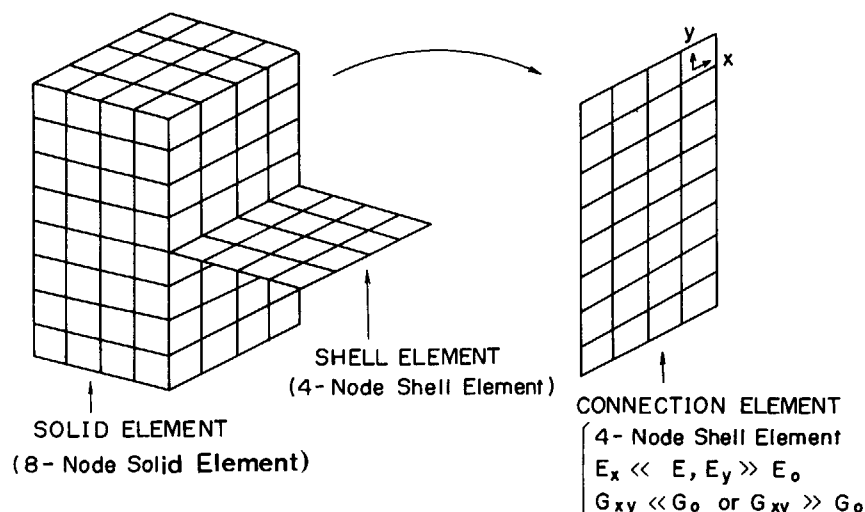

SHELL ELEMENT
(4-Node Shell Element)

SOLID ELEMENT
(8-Node Solid Element)

CONNECTION ELEMENT
⎡ 4-Node Shell Element
| $E_x \ll E, E_y \gg E_o$
⎣ $G_{xy} \ll G_o$ or $G_{xy} \gg G_o$

Fig. 3.1.4 Finite element mesh of CASE 7.

$$
\begin{cases}
E_x = 10^{-3} E_0 \\
E_y = 10^{-3} E_0 \\
G_{xy} = 10^{-3} G_0 \text{ or } G_{xy} = 10^{3} G_0 \\
v_{xy} = 0
\end{cases}
$$

in which E, G and v are the modulus of elasticity, the shearing modulus of elasticity and Poisson's ratio, respectively, and subscript 0 denotes the value related to the base material.

Table 3.1.1   Comparison of displacements among various methods for loading condition LC-1
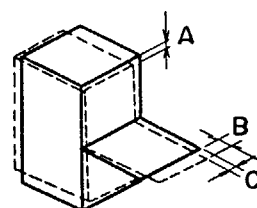
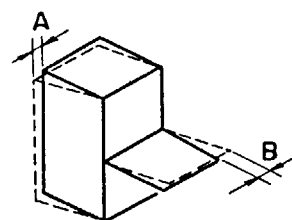| CASE NO.	DISPLACEMENT (mm)		
	A	B	C
Exact	-1.5000×10^{-5}	5.0000×10^{-5}	-7.5000×10^{-6}
1	-1.5000×10^{-5}	5.0000×10^{-5}	-7.5000×10^{-6}
2	-1.5000×10^{-5}	5.0000×10^{-5}	-7.5000×10^{-6}
3	-1.5000×10^{-5}	5.0000×10^{-5}	-7.5000×10^{-6}
4	-1.5000×10^{-5}	5.0000×10^{-5}	-7.5000×10^{-6}
5	-2.8580×10^{-5}	6.6010×10^{-5}	-7.4434×10^{-6}
6	-1.0269×10^{-5}	5.1188×10^{-5}	-7.5460×10^{-6}
7	0.0	5.01×10^{-5}	-7.7×10^{-6}

Table 3.1.2   Comparison of displacements among various methods for loading condition LC-2
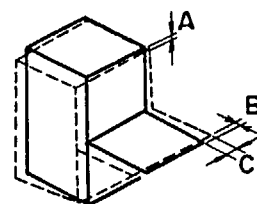
CASE NO.	DISPLACEMENT (mm)		
	A	B	C
Exact	-1.5000×10^{-5}	-1.5000×10^{-5}	2.5000×10^{-5}
1	-1.5000×10^{-5}	-1.5000×10^{-5}	2.5000×10^{-5}
2	-1.5000×10^{-5}	-1.5000×10^{-5}	2.5000×10^{-5}
3	-1.5000×10^{-5}	-1.5000×10^{-5}	2.5000×10^{-5}
4	-1.5000×10^{-5}	-1.5000×10^{-5}	2.5000×10^{-5}
5	-1.5000×10^{-5}	-1.5000×10^{-5}	2.5000×10^{-5}
6	-1.4843×10^{-5}	-1.4937×10^{-5}	2.5200×10^{-5}
7	-2.0×10^{-8}	-1.48×10^{-5}	2.5×10^{-5}

Tables 3.1.1 ~ 3.1.6 show the comparison of displacements among various methods. It is found from the tables that the connection elements in the EPAS-J1 program provide good agreements with the theoretical values for the loading conditions of LC-1 ~ LC-3. On the other hand, for the loading conditions of LC-4 ~ LC-6, some differences are found between the results obtained from the analyses using the connection elements and the theoretical values. However, comparing the results of CASE 1 ~ CASE 5 with those of CASE 6 and CASE 7, the connection elements included in the EPAS-J1 program provide more accurate displacements than other methods such as using the linear constraint equations and the anisotropic flat shell element. **Tables 3.1.7 ~ 3.1.12** show the comparison of stresses among various methods. For the loading conditions of LC-1 ~ LC-3, the results of CASE 1 ~ CASE 3 where all solid


Table 3.1.3 Comparison of displacements among various methods for loading condition LC-3

CASE NO.	DISPLACEMENT (mm)		
	A	B	
Exact	-1.3000×10^{-4}	1.3000×10^{-4}	
1	-1.3000×10^{-4}	1.3000×10^{-4}	
2	-1.3000×10^{-4}	1.3000×10^{-4}	
3	-1.3000×10^{-4}	1.3000×10^{-4}	
4	-1.3000×10^{-4}	1.3000×10^{-4}	
5	-1.6714×10^{-4}	1.3079×10^{-4}	
6	-3.0903×10^{-4}	1.2788×10^{-4}	
7	-1.3×10^{-4}	1.3×10^{-4}	$\leftarrow G_{xy} \gg G_o$
	-2.93×10^{-4}	1.32×10^{-4}	$\leftarrow G_{xy} \ll G_o$

**Table 3.1.4** Comparison of displacements among various methods for loading condition LC-4
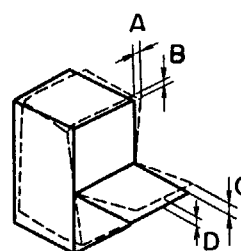
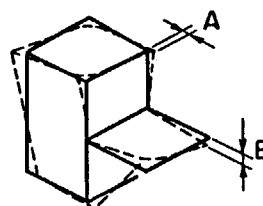| CASE NO.	DISPLACEMENT (mm)			
	A	B	C	D
Exact	7.5000×10^{-6}	7.5000×10^{-6}	2.3100×10^{-5}	2.5000×10^{-5}
1	1.1575×10^{-5}	1.0590×10^{-5}	2.3177×10^{-5}	2.5060×10^{-5}
2	1.0728×10^{-5}	1.0939×10^{-5}	2.3080×10^{-5}	2.4969×10^{-5}
3	1.0651×10^{-5}	2.3686×10^{-5}	2.3189×10^{-5}	2.5075×10^{-5}
4	1.0059×10^{-5}	2.4703×10^{-5}	2.2979×10^{-5}	2.4869×10^{-5}
5	1.0505×10^{-5}	2.5965×10^{-5}	2.2958×10^{-5}	2.4848×10^{-5}
6	8.6425×10^{-5}	5.7342×10^{-6}	2.9006×10^{-5}	3.0750×10^{-5}
7	8.8×10^{-6}	1.9×10^{-6}		2.42×10^{-5}

elements in the connection plane are connected to the flat shell elements are identical with the theoretical values, while those of CASE 5 where the solid elements in the connection plane are partially connected to the flat shell elements does not completely agree with the theoretical values. Even in the latter case, however, the further element from the connection plane, elem. 2, gives better results than the element adjacent to the connection plane, elem. 10. The same tendency can be also found for the loading conditions of LC-4 ∼ LC-6. This means that the disturbance of stress distribution is localized near the connection plane. Generally speaking, the connection elements in the EPAS-J1 program provide more accurate stress than the others.

Table 3.1.5 Comparison of displacements among various methods for loading condition LC-5
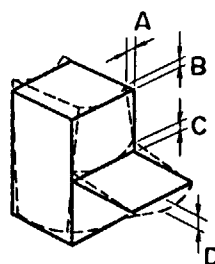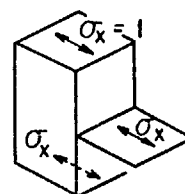
CASE NO.	DISPLACEMENT (mm)			
	A	B	C	D
Exact	-2.5000×10^{-5}	7.5000×10^{-6}	6.2500×10^{-6}	-7.5000×10^{-6}
1	-2.4739×10^{-5}	1.1781×10^{-5}	6.2448×10^{-6}	-7.4955×10^{-6}
2	-2.4805×10^{-5}	1.1796×10^{-5}	6.2436×10^{-6}	-7.4980×10^{-6}
3	-2.5000×10^{-5}	1.2292×10^{-5}	6.2500×10^{-6}	-7.4999×10^{-6}
4	-2.5000×10^{-5}	1.2292×10^{-5}	6.2500×10^{-6}	-7.4999×10^{-6}
5	-2.5000×10^{-5}	1.2292×10^{-5}	6.2500×10^{-6}	-7.4999×10^{-6}
6	-2.4861×10^{-5}	1.6543×10^{-5}	6.1761×10^{-6}	-7.4617×10^{-6}
7	-2.1×10^{-5}	6.2×10^{-6}	0	-7.46×10^{-6}

Table 3.1.6 Comparison of displacements among various methods for loading condition LC-6

CASE NO.	DISPLACEMENT (mm)	
	A	B
Exact	6.5000×10^{-5}	-6.5000×10^{-5}
1	4.4983×10^{-5}	-3.7407×10^{-5}
2	4.0053×10^{-5}	-4.0041×10^{-5}
3	4.7900×10^{-5}	-3.7382×10^{-5}
4	4.1774×10^{-5}	-4.0055×10^{-5}
5	4.1217×10^{-5}	-4.0162×10^{-5}
6	7.0929×10^{-6}	-2.6495×10^{-5}
7	2.0×10^{-7}	-2.4×10^{-5} ← $G_{xy} \gg G_o$
	5.3×10^{-5}	-3.8×10^{-4} ← $G_{xy} \ll G_o$

Table 3.1.7 Comparison of stresses among various
methods for loading condition LC-1

CASE NO.	STRESS (kg/mm^2)		
	Solid (elem. 2)	Solid (elem. 10)	Shell
Exact	σ_x=1.0000	σ_x=1.0000	σ_x=1.0000
1	1.0000 (G1) 1.0000 (G2) 1.0000 (G3)	1.0000 (G1) 1.0000 (G2) 1.0000 (G3)	1.0000
2	1.0000 (G1) 1.0000 (G2) 1.0000 (G3)	1.0000 (G1) 1.0000 (G2) 1.0000 (G3)	1.0000
3	1.0000 (G1) 1.0000 (G2) 1.0000 (G3)	1.0000 (G1) 1.0000 (G2) 1.0000 (G3)	1.0000
4	1.0000 (G1) 1.0000 (G2) 1.0000 (G3)	1.0000 (G1) 1.0000 (G2) 1.0000 (G3)	1.0000
5	0.9711 (G1) 0.9315 (G2) 0.9270 (G3)	1.2311 (G1) 1.0464 (G2) 0.7977 (G3)	1.0000
6	0.9456 (G1) 0.8585 (G2) 0.7934 (G3)	1.2728 (G1) 1.2545 (G2) 1.1484 (G3)	1.0000
7	1.1	1.1	0.997

Table 3.1.8 Comparison of stresses among various methods for loading condition LC-2
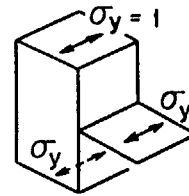
CASE NO.	STRESS (kg/mm²)			
	Solid (elem. 2)	Solid (elem. 10)	Shell (elem. 18)	Shell (elem. 20)
Exact	σ_y=1.0000	σ_y=1.0000	σ_y=1.0000	σ_y=1.0000
1	1.0000 (G1) 1.0000 (G2) 1.0000 (G3)	1.0000 (G1) 1.0000 (G2) 1.0000 (G3)	1.0000	1.0000
2	1.0000 (G1) 1.0000 (G2) 1.0000 (G3)	1.0000 (G1) 1.0000 (G2) 1.0000 (G3)	1.0000	1.0000
3	1.0000 (G1) 1.0000 (G2) 1.0000 (G3)	1.0000 (G1) 1.0000 (G2) 1.0000 (G3)	1.0000	1.0000
4	1.0000 (G1) 1.0000 (G2) 1.0000 (G3)	1.0000 (G1) 1.0000 (G2) 1.0000 (G3)	1.0000	1.0000
5	1.0000 (G1) 1.0000 (G2) 1.0000 (G3)	1.0000 (G1) 1.0000 (G2) 1.0000 (G3)	1.0000	1.0000
6	0.9871 (G1) 1.0122 (G2) 1.0312 (G3)	1.0180 (G1) 0.9507 (G2) 0.8913 (G3)	0.9289	1.0079
7	0.897	0.995	0.992	1.02

Table 3.1.9 Comparison of stresses among various
methods for loading condition LC-3
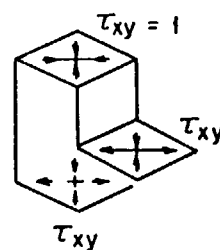
CASE NO.	STRESS (kg/mm^2)		
	Solid (elem. 2)	Solid (elem. 10)	Shell
Exact	$\tau_{xy}=1.0000$	$\tau_{xy}=1.0000$	$\tau_{xy}=1.0000$
1	1.0000 (G1) 1.0000 (G2) 1.0000 (G3)	1.0000 (G1) 1.0000 (G2) 1.0000 (G3)	1.0000
2	1.0000 (G1) 1.0000 (G2) 1.0000 (G3)	1.0000 (G1) 1.0000 (G2) 1.0000 (G3)	1.0000
3	1.0000 (G1) 1.0000 (G2) 1.0000 (G3)	1.0000 (G1) 1.0000 (G2) 1.0000 (G3)	1.0000
4	1.0000 (G1) 1.0000 (G2) 1.0000 (G3)	1.0000 (G1) 1.0000 (G2) 1.0000 (G3)	1.0000
5	1.0289 (G1) 0.9910 (G2) 0.9457 (G3)	0.9994 (G1) 0.7722 (G2) 0.5988 (G3)	1.0000
6	1.0225 (G1) 0.9375 (G2) 0.8572 (G3)	0.5985 (G1) 0.4995 (G2) 0.3180 (G3)	1.0000
7			1.0

Table 3.1.10　Comparison of stresses among various methods for loading condition LC-4
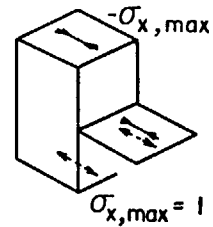
CASE NO.	STRESS (kg/mm^2)			
	Solid (elem. 2)	Solid (elem. 10)	Solid (Top Surface)	Shell
Exact	$\sigma_x = -0.9436$	$\sigma_x = -0.9436$	$\sigma_x = -0.8750$	$\sigma_x = -1.0000$
1	−0.9693 (G1) −1.0661 (G2) −1.1744 (G3)	−1.2765 (G1) −1.6120 (G2) −1.8321 (G3)		−1.0000
2	−0.9690 (G1) −1.0651 (G2) −1.1733 (G3)	−1.2705 (G1) −1.6171 (G2) −1.8520 (G3)		−1.0000
3	−0.9132 (G1) −0.9910 (G2) −1.1011 (G3)	−1.7415 (G1) −2.2270 (G2) −2.3028 (G3)		−1.0000
4	−0.9113 (G1) −0.9897 (G2) −1.1011 (G3)	−1.7534 (G1) −2.2680 (G2) −2.3634 (G3)		−1.0000
5	−0.9089 (G1) −0.9898 (G2) −1.1039 (G3)	−1.7594 (G1) −2.2657 (G2) −2.3541 (G3)		−1.0000
6	−0.9676 (G1) −0.9900 (G2) −0.10089 (G3)	−0.9419 (G1) −0.8944 (G2) −0.8822 (G3)		−1.0000
7			−0.844	

Table 3.3.11   Comparison of stresses among various methods for loading condition LC-5

$\sigma_{y,max} = 1$

CASE NO.	STRESS (kg/mm^2)				
	Solid (elem. 2)	Solid (elem. 10)	Solid (Top Surface)	Shell (elem. 17 18)	Shell (elem. 19 20)
Exact	σ_y=−0.9436	σ_x=−0.9436	σ_y=−0.8750	σ_x=−1.0000	σ_y=−1.0000
1	−0.9564 (G1) −0.9561 (G2) −0.9567 (G3)	−0.9565 (G1) −0.9560 (G2) −0.9571 (G3)		−0.9994	−0.9999
2	−0.9565 (G1) −0.9560 (G2) −0.9566 (G3)	−0.9563 (G1) −0.9564 (G2) −0.9593 (G3)		−0.9990	−0.9998
3	−0.9436 (G1) −0.9436 (G2) −0.9436 (G3)	−0.9436 (G1) −0.9436 (G2) −0.9436 (G3)		−1.0000	−1.0000
4	−0.9436 (G1) −0.9436 (G2) −0.9436 (G3)	−0.9436 (G1) −0.9436 (G2) −0.9436 (G3)		−1.0000	−1.0000
5	−0.9436 (G1) −0.9436 (G2) −0.9436 (G3)	−0.9436 (G1) −0.9436 (G2) −0.9436 (G3)		−1.0000	−1.0000
6	−0.9582 (G1) −0.9555 (G2) −0.9555 (G3)	−0.9436 (G1) −0.9436 (G2) −0.9436 (G3)		−0.9940	−0.9979
7			−0.814		

$$\tau_{xy,max} = 1$$

$$-\tau_{xy,max}$$

Table 3.1.12 Comparison of stresses among various methods for loading condition LC-6

CASE NO.	STRESS (kg/mm²)				
	Solid (elem. 2)	Solid (elem. 10)	Solid (Top Surface)	Shell (elem. 17 18)	Shell (elem. 19 20)
Exact	τ_{xy}=0.9436	τ_{xy}=0.9436	τ_{xy}=0.8750	τ_{xy}=1.0000	τ_{xy}=1.0000
1	0.9145 (G1) 0.9406 (G2) 0.9708 (G3)	1.1012 (G1) 1.2097 (G2) 1.2691 (G3)		0.8711	0.8599
2	0.9399 (G1) 0.9550 (G2) 0.9704 (G3)	1.0473 (G1) 1.1017 (G2) 1.1540 (G3)		0.8036	0.8652
3	0.9026 (G1) 0.9413 (G2) 0.9869 (G3)	1.3114 (G1) 1.3927 (G2) 1.4202 (G3)		0.8776	0.8594
4	0.9327 (G1) 0.9582 (G2) 0.9866 (G3)	1.1991 (G1) 1.2319 (G2) 1.2509 (G3)		0.8158	0.8653
5	0.9326 (G1) 0.9585 (G2) 0.9852 (G3)	1.2004 (G1) 1.2243 (G2) 1.2381 (G3)		0.8096	0.8655
6	0.9674 (G1) 0.9642 (G2) 0.9510 (G3)	0.7610 (G1) 0.5141 (G2) 1.1846 (G3)		0.8862	0.7981
7			0.705 0.504	$\leftarrow G_{xy} \gg G_o$ $\leftarrow G_{xy} \ll G_o$	

3.2 Numerical Tests on Virtual Crack Extension Method

3.2.1 Two-dimensional Crack Prohelm

The results are shown for the two-dimensional crack problem analyzed by the virtual crack extension method. **Figure 3.2.1** shows the centrally cracked plate under uniform tension which was treated as a plane stress problem. One quarter of the plate was taken due to the symmetry of the structure. **Figure 3.2.2** shows the two patterns of the finite element mesh. The 8-node elements (PLANE8) are used in the analysis. The mid-nodes of the two elements allocated at the crack tip were shifted at the quarter points. Singularity of the stress field around the crack tip can be taken into accounts by this type of the element called 'distorted element'. **Figure 3.2.3** shows the two cases of the method of advancing the crack tip node. Namely, only one node at the crack tip was advanced by Δa in CASE 1, whereas three
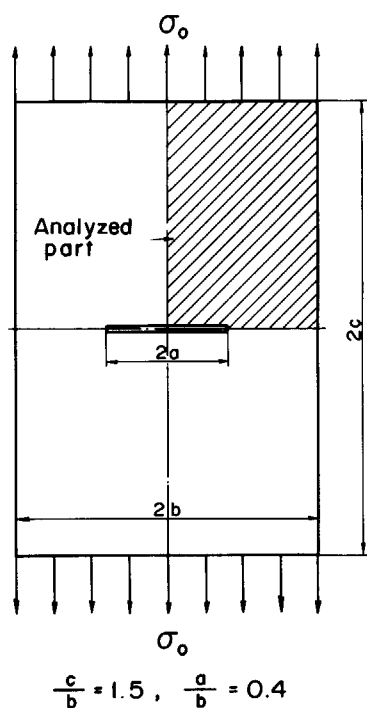
$$\frac{c}{b} = 1.5, \quad \frac{a}{b} = 0.4$$

Fig. 3.2.1 Centrally cracked plate under uniform tension.

MODEL 1   MODEL 2

Fig. 3.2.2 Finite element mesh for one quarter of cracked plate.

CASE 1   CASE 2
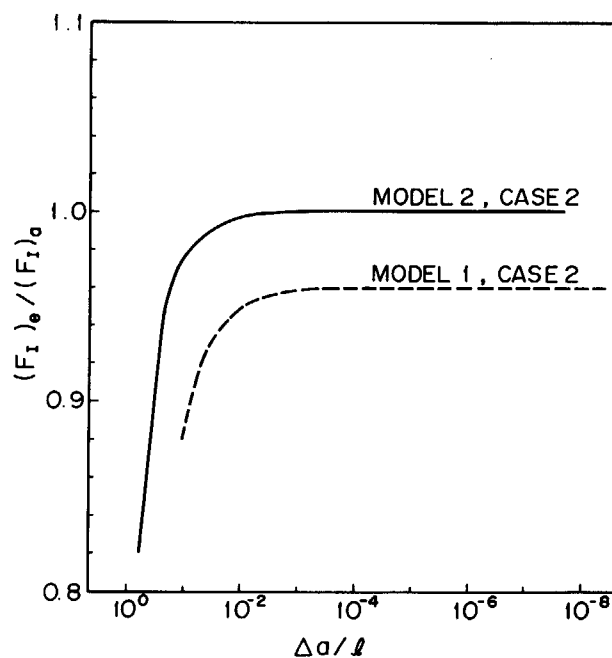
Fig. 3.2.3 Method of advancing crack tip node.

Fig. 3.2.4 Nondimensional stress intensity factor vs. virtual crack extension value.

quarter-point nodes around the crack were advanced by Δa in CASE 2. The curves of nondimensional stress intensity factor vs. virtual crack extension value are shown in **Fig. 3.2.4** where ℓ denotes the side length of the element measured in the direction of crack extension. F_I is the nondimensional stress intensity factor defined by

$$F_I = \frac{K_I}{\sigma_0 \sqrt{\pi a}}$$

and the subscripts e and a represent the values obtained by the present method and Ishida[16], respectively. It can be seen from the figure that the convergent stress intensity factors are

obtained for both MODEL 1 and MODEL 2 when $\Delta a/\ell$ is smaller than the value of 10^{-2}. Especially, the convergent solution of MODEL 2 is almost coincident with that of Ishida which is regarded as an exact solution. The accuracy of solution is sharply deteriorated when $\Delta a/\ell$ is larger than the value of 10^{-2} due to the reason that the derivative of the stiffness matrix contained in eq. (2.3.9) cannot be accurately estimated. On the other hand, the accuracy of solution is also thought to be detriorated due to the round-off error, when $\Delta a/\ell$ is relatively small compared with the number of digits which the computer used in the calculation can represent. In this analysis, deterioration of accuracy cannot be found even at $\Delta a/\ell$ of 10^{-8}, because CDC 6600 machine used in the analysis has 60 bits per one word. According to Hellen's analysis[8], deterioration of accuracy could be found when $\Delta a/\ell$ was smaller than the value of 10^{-4}, since the computer used had 32 bits per one word which could represent only the six or seven digits.

Table 3.2.1 shows the nondimensional stress intensity forctor for each case and each model. As stated above, the results of MODEL 1 are coincident with that of Ishida for both CASE 1 and 2. On the other hand, it is notable that the difference is only 4 ~ 6% between the result of Ishida and that of MODEL 1 where relatively coarse mesh was employed. Comparing two types of the methods of advancing crack, CASE 2 gives better results than CASE 1. However, the difference between CASE 1 and 2 becomes small when the size of the crack tip element becomes small.

Table 3.2.1 Nondimensional stress intensi-
ty factor for centrally cracked
plate under uniform tension

	CASE NO.	F_I	$(F_I)_e/(F_I)_a$
MODEL 1	1	1.057	0.942
	2	1.077	0.960
MODEL 2	1	1.120	0.998
	2	1.123	1.001
Ishida's Sol.		1.122	

$(F_I)_e$ = F_I of Finite Element Method
$(F_I)_a$ = F_I of Analytical Solution (Ishida's Sol.)

3.2.2 Three-dimensional Crack Problem

The stress intensity factor analyses were performed using the 16-node and 20-node solid elements for some simple three-dimensional structures to confirm the accuracy of the virtual crack extension method.

[I] Three-dimensional Analysis of Compact Tension Specimen

An analysis was performed to obtain the thickness distribution of the stress intensity factor of a compact tension specimen shown in **Fig. 3.2.5** using SOLID16 and SOLID20 elements. The dimensions of the compact tension specimen and the loading applied to the specimen are given in **Fig. 3.2.5**. One quarter of the specimen was taken due to the symmetry of the structure. **Figure 3.2.6** shows the finite element model of the compact tension specimen. The same finite element model was used in the analyses using SOLID16 and SOLID20 elements. The three-dimensional distorted elements were allocated along the crack front to take account of the singularity of the stress around the crack tip.

Figure 3.2.7 shows the ratio of the incremental potential energy $\Delta \pi$ to the virtual crack extension value Δy vs. nondimensional virtual crack extension value $\Delta y/\ell$ in which ℓ denotes
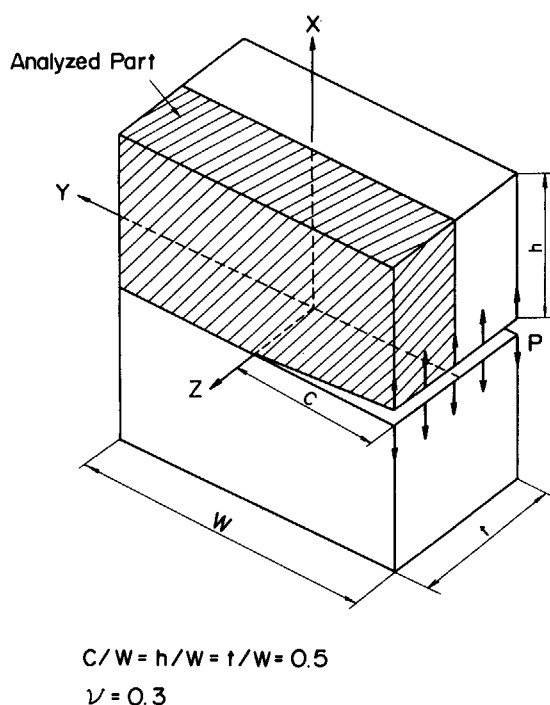
Fig. 3.2.5   Compact tension specimen.

$C/W = h/W = t/W = 0.5$
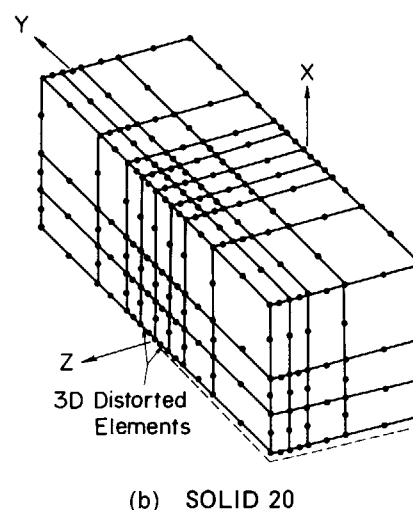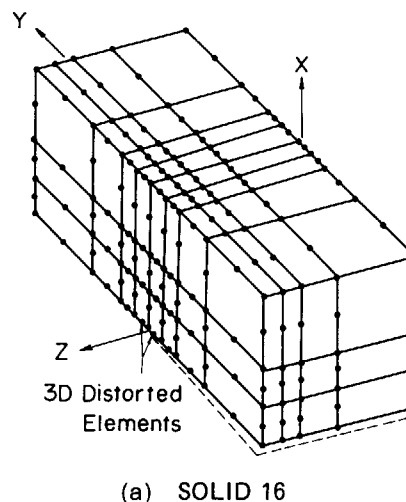
$\nu = 0.3$

(a)   SOLID 16

(b)   SOLID 20

Fig. 3.2.6   Finite element mesh of compact
tension specimen.

the side length of the element measured in the direction of the y-axis in **Fig. 3.2.5**. It is shown in the figure that $\Delta\pi/\Delta y$ is constant when $\Delta y/\ell$ is smaller than the value of 10^{-3}. Large difference is seen between the results of the mid- and corner-nodes of SOLID20 element.

The thickness distribution of the nondimensional stress intensity factor F obtained by the analysis is given in **Fig. 3.2.8** where the results obtained by Yagawa et al.[17], Reynen[1] and Tracey[18] are also depicted. Yagawa et al. proposed the method based on the discretization error of the finite element technique and obtained the accurate stress intensity factor. Reynen applied the virtual crack extension method to the BERSAFE code, together with the substructuring technique. It is, however, not clear whether the element allocated along the crack front was the 16-node or 20-node solid elements. Tracey utilized the direct method based on the displacements and the stresses obtained from the finite element analysis using the 6-node prismatic singular element developed by himself. The load in the analyses by Reynen and Tracey was the same as that of the present analysis, while in the analysis by Yagawa et al. the load was applied at the location distant by $h/2$ from the crack edge. The present solution with SOLID16 gives smooth stress intensity factor throughout the thickness and lies between other three solutions. On the other hand, large discrepancy is found in the present method between the stress intensity factors obtained from the mid- and corner-nodes of SOLID20 element used in the present analysis. It is, therefore, required in the case of SOLID20 element either to average the values of the mid- and corner-nodes or to employ one of two values,
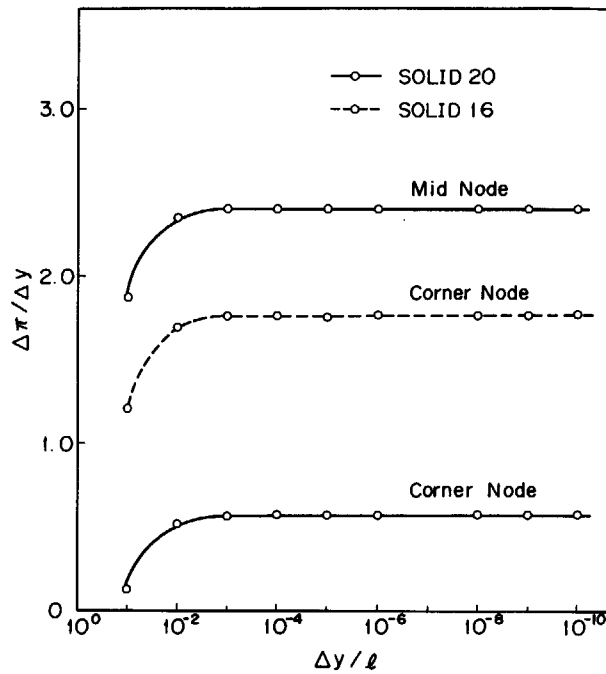
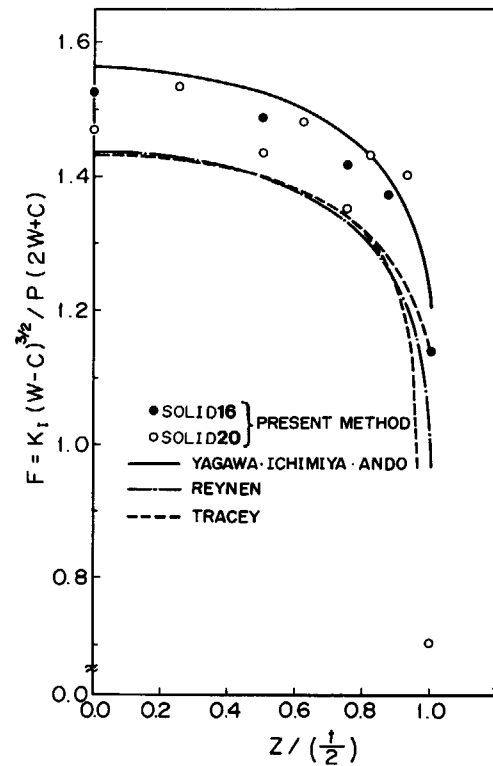**Fig. 3.2.7** Energy release rate vs. virtual crack extension value.

Fig. 3.2.8 Thickness distribution of non-dimensional stress intensity factors for compact tension specimen.

based on reasonable judgement. From this reason, SOLID16 element is recommended for the stress intensity factor analysis using the virtual crack extension method.

[II] Surface Crack Problem

Next, let us consider the problem of obtaining the stress intensity factor for the semi-circular surface crack in a finite plate subjected to a uniform tension σ_0 as shown in **Fig.**
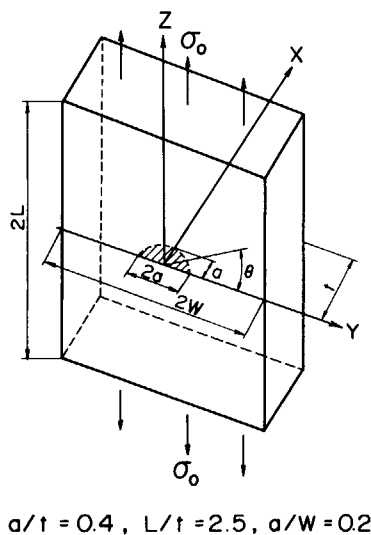
$a/t = 0.4$, $L/t = 2.5$, $a/W = 0.2$

Fig. 3.2.9 Plate with semi-circular surface crack.
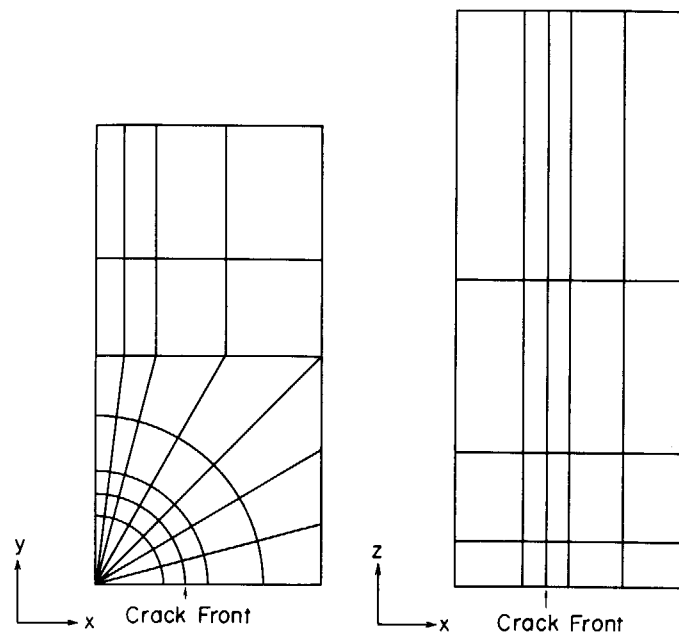

Crack Front　　　　　Crack Front

Fig. 3.2.10 Finite element mesh of surface crack problem.

3.2.9. The configuration of the plate is also given in **Fig. 3.2.9**. Poisson's ratio was assumed to be 0.3. The finite element mesh of one quarter of the plate and the node allocation are given in **Fig. 3.2.10** and **Fig. 3.2.11**, respectively. The distorted elements were allocated along the crack front to take account of the sigularity of the stress around the crack tip. The analyses were carried out using SOLID16 and SOLID20 elements, together with the virtual crack extension value Δa of 4×10^{-7} ℓ, where ℓ denotes the length of the crack element.

Figure 3.2.12 shows the peripheral distribution of nondimensional stress intensity factors obtained by the EPAS-J1 code. In the figure, M denotes the non-dimensional stress intensity
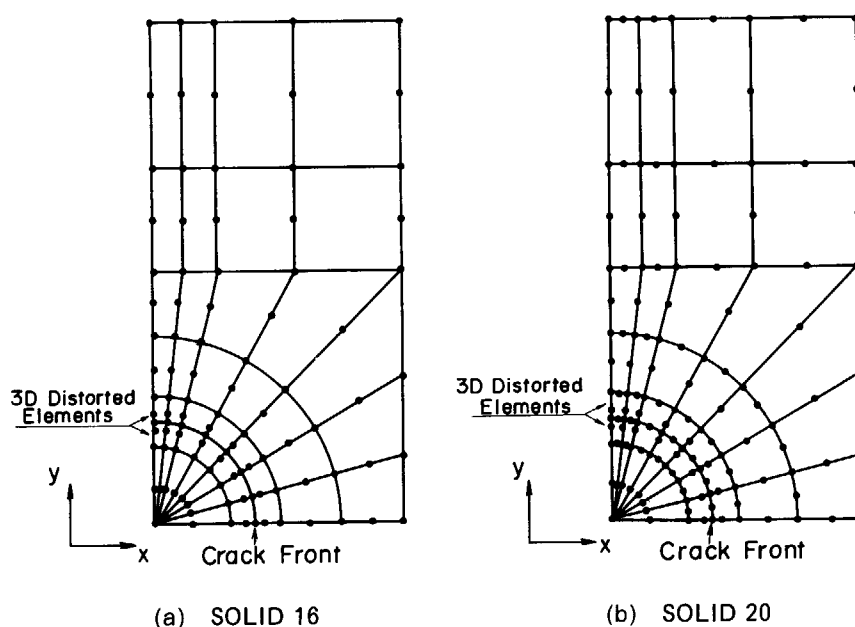

(a) SOLID 16   (b) SOLID 20

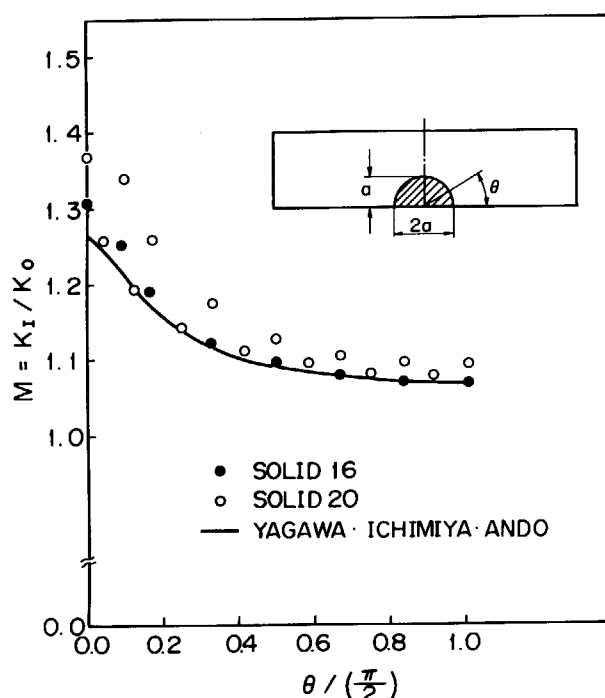**Fig. 3.2.11**   Node allocations of surface crack problem.

Fig. 3.2.12   Peripheral distribution of nondimensional stress intensity factors
for semi-circular surface crack.

factor defined by

$$M = K_I/K_0$$

$$K_0 = 2\sigma_0 \sqrt{a/\pi}$$

where K_0 is the stress intensity factor of a circular crack with radius a in a infinite plate subjected to a stress σ_0. Yagawa *et al.'s* solution is also depicted in the figure for comparison. The present analysis using SOLID16 element gives about 3.5 percent larger value at $\theta/(\frac{\pi}{2}) = 0.0$ than Yagawa *et al.'s* solution, but both are almost coincident in the region where $\theta/(\frac{\pi}{2})$ is larger than 0.5. On the other hand, there is large difference between the results obtained from mid- and corner-nodes in the present analysis using SOLID20 element, which was also found in the case of the stress intensity factor analysis of the compact tension specimen presented in [I] in this section. Therefore, it can be concluded that SOLID16 element should be used to obtain the stress intensity factors of the three-dimensional cracks.

3.3 Stress Intensity Factor Analyses of Three-dimensional Surface Cracks

In this section are presented the results of the stress intensity factor analyses for a pressurized cylinder with an outer semi-elliptical crack, a cylinder with a single surface crack or nearly-located three surface cracks subjected to shear force. In the analyses, the connection elements were used to connect different kinds of elements such as the beam, shell and solid elements.

3.3.1 Longitudinal Semi-elliptical Crack in Outer Surface of a Pressurized Cylinder

Consider a pressurized cylinder with an outer semi-elliptical crack shown in **Fig. 3.3.1** whose solutions were obtained by Atluri and Kathiresan[20], Blackburn and Hellen[21], and Kobayashi, *et al.*[22]. The dimensions of the cylinder and Poisson's ratio ν used in the analysis are as follows:

$$R_o/R_i = 1.5, \quad b/a = 0.6, \quad b/(R_o - R_i) = 0.4,$$

$$L = 480 \text{ mm}, \quad R_i = 120 \text{ mm}, \quad R_o = 180 \text{ mm},$$

$$a = 40 \text{ mm}, \quad b = 24 \text{ mm}, \quad \nu = 0.3$$

The finite element model used in the analysis is given in **Fig. 3.3.2**. One quarter of the structure was taken due to the symmetry of the structure. The 16-node solid elements (SOLID16) were used in the neighborhood of the crack and the remainder of the cylinder was modeled by the 4-node thin shell elements (FSHEL4). The 8-node connection elements (BOUND8) were used to connect these two kinds of elements. In addition to internal pressure, the axial force corresponding to internal pressure was assumed to act upon the cylinder to take account of the end effect of internal pressure. The shell element is thought to be more flexible under internal pressure than the solid element, because the shell element has larger area per unit circumferential angle subjected to internal pressure than the solid element. Therefore, a preliminary calculation was carried out to study the methods for loading of internal pressure. For this purpose, analyses were performed for the cylinder without crack whose inner and outer diameters were same as the cylinder shown in **Fig. 3.3.1** and whose length was 120 mm. Only the region from 0° to 90° of the cylinder was taken due to the symmetry of the structure. The solid elements (SOLID16), the shell elements (FSHEL4) and the solid-shell connection elements (BOUND8) were used to model the cylinder as shown in **Fig. 3.3.3**. The following three cases were considered for the loading of internal pressure.

LC-1:   Same internal pressure 1.0 P_i kg/mm² was loaded on both solid and shell regions.

LC-2:   Considering the difference in area per unit circumferential angle between the solid and shell elements, 1.2 P_i and 1.0 P_i were loaded on the solid and shell regions, respectively.
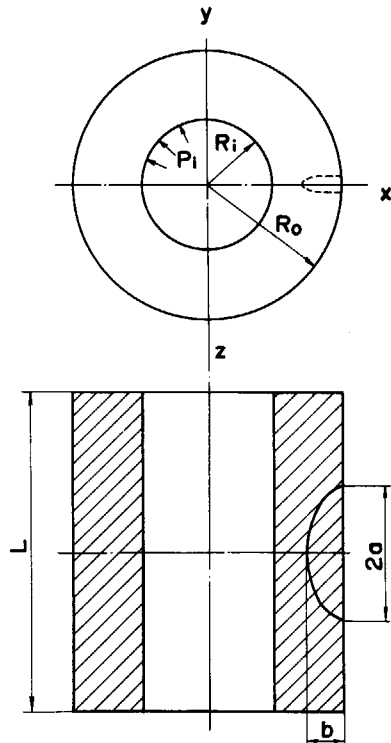

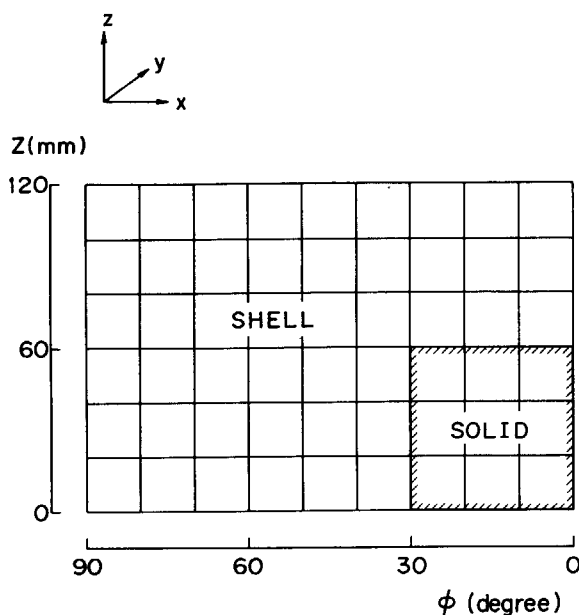**Fig. 3.3.1**   A pressurized cylinder with outer semi-elliptical crack.

Fig. 3.3.2   Analytical model of a pressurized cylinder with outer semi-elliptical crack.

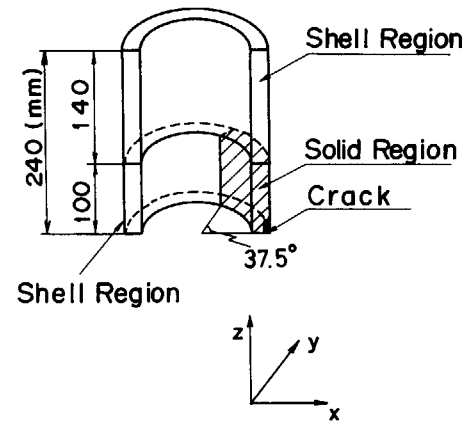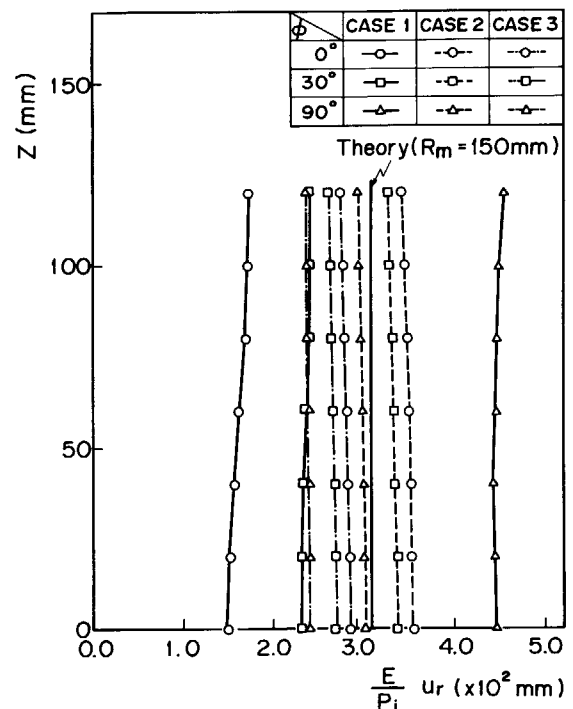**Fig. 3.3.3**   Finite element mesh of a pressurized cylinder without crack.

Fig. 3.3.4   Distribution of radial displacements U_r along z-axis for a pressurized cylinder without crack.

LC-3 :   1.0 P_i and 0.8 P_i were loaded on the solid and shell regions, respectively, based
on the same reason as in LC-2.

Figures 3.3.4 and **3.3.5** show the distributions of radial displacement U_r along z-axis and
circumferential direction, respectively. In the figures, the solid lines show the exact solution
for the displacement in the mid-thickness of the cylinder. Large displacement is caused in the
shell region, since relatively large load acts upon this region. Compared with the exact solution,
LC-2 gives better results than LC-3. This is due to the reason that LC-2 can represent the
displacement behavior of the thick cylinder subjected to internal pressure based on the thin
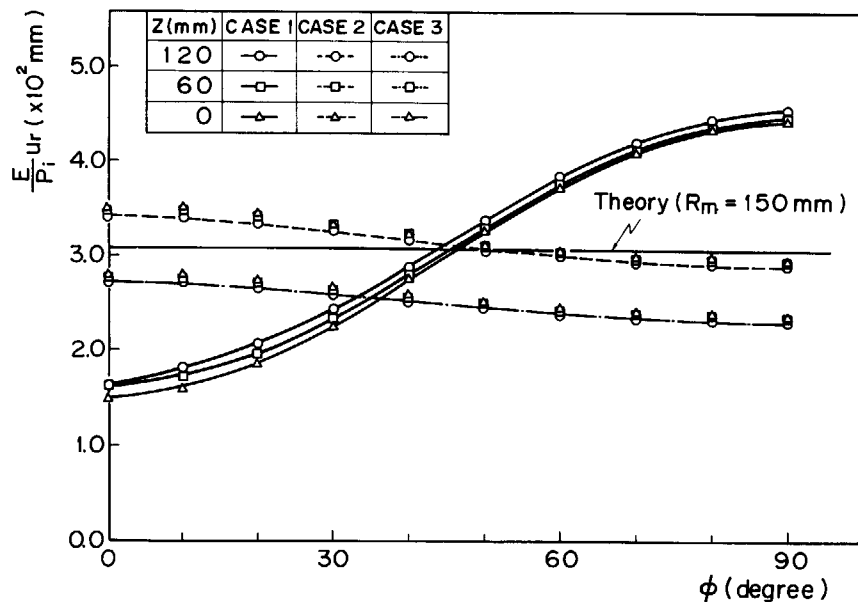shell theory. Therefore, the loading condition of LC-2 was employed for the present analysis.

Fig. 3.3.5 Distribution of radial displacements U_r along circumference for a pressurized
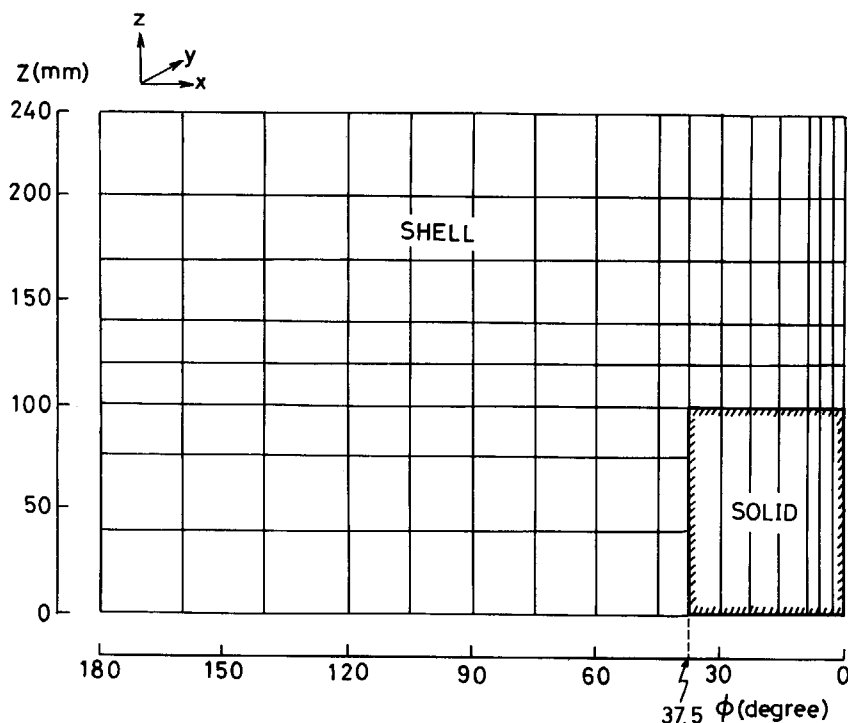cylinder without crack.

Fig. 3.3.6 Finite element mesh of a pressurized cylinder with outer semi-elliptical crack.

Figure 3.3.6 shows the finite element model of a pressurized cylinder in the development figure. **Figure 3.3.7** also shows the finite element mesh in the surface with the crack. In the analysis, the distorted elements were allocated along the crack front. The numbers of each element, nodes and total degrees-of-freedom used in the analysis, are given in **Table 3.3.1**. **Figures 3.3.8** and **3.3.9** show the distributions of the radial displacement along the z-axis and circumferential direction, respectively. From the figures, good agreement is found between the present solution and exact one regarding to the displacement far from the crack. On the other
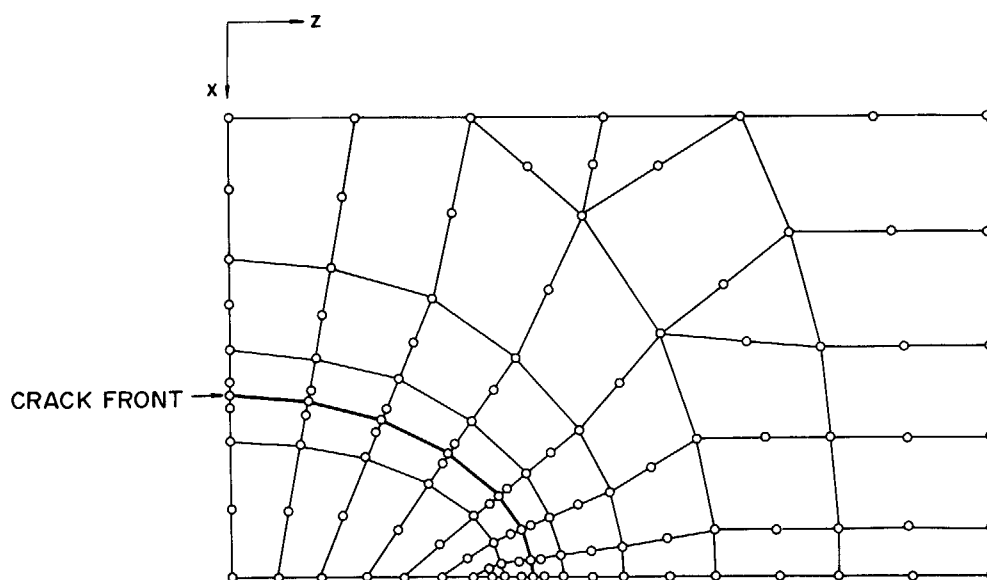

Fig. 3.3.7 Finite element mesh in the surface with crack.
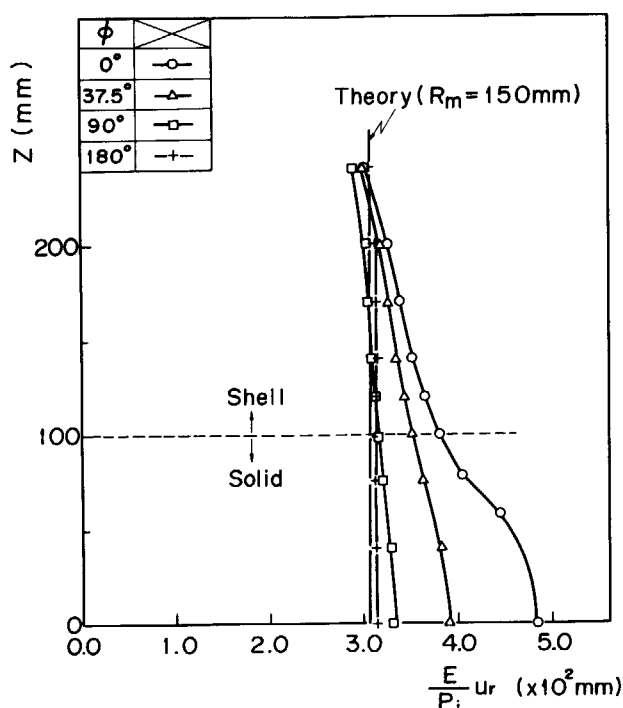
Fig. 3.3.8 Distribution of radial displacements U_r along z-axis for a pressurized cylinder with outer semi-elliptical crack.

Table 3.3.1 Numbers of elements, nodes and degrees-of-freedom for the stress intensity factor analysis of a pressurized cylinder with a semi-elliptical crack

Number of Elements	
SOLID16	229
FSHEL4	107
BOUND8	46
Number of Nodes	1,456
Number of Degrees-of-freedom	4,830

hand, large displacement is found near the crack, since stiffness decreases locally in the neighborhood of the crack. It is also found that displacement varies smoothly at the boundary of the solid and shell elements.

Figure 3.3.10 shows the peripheral distribution of the nondimensional stress intensity factor normalized by the following closed form solution K_0 of the elliptical crack embedded in an infinite body subjected to an uniform tensile stress σ_0 :
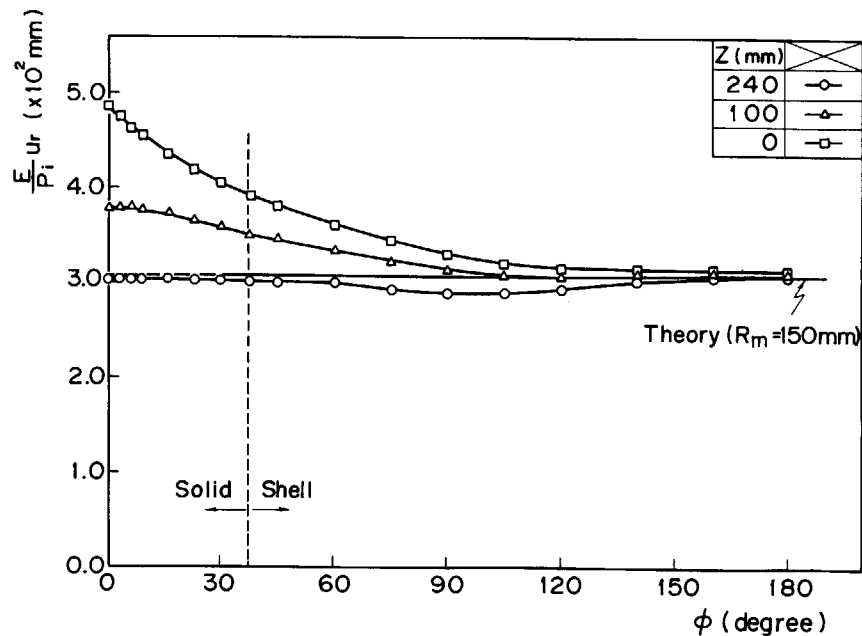

Fig. 3.3.9   Distribution of radial displacement U_r along cicumference for a pressurized cylinder with outer semi-elliptical crack.
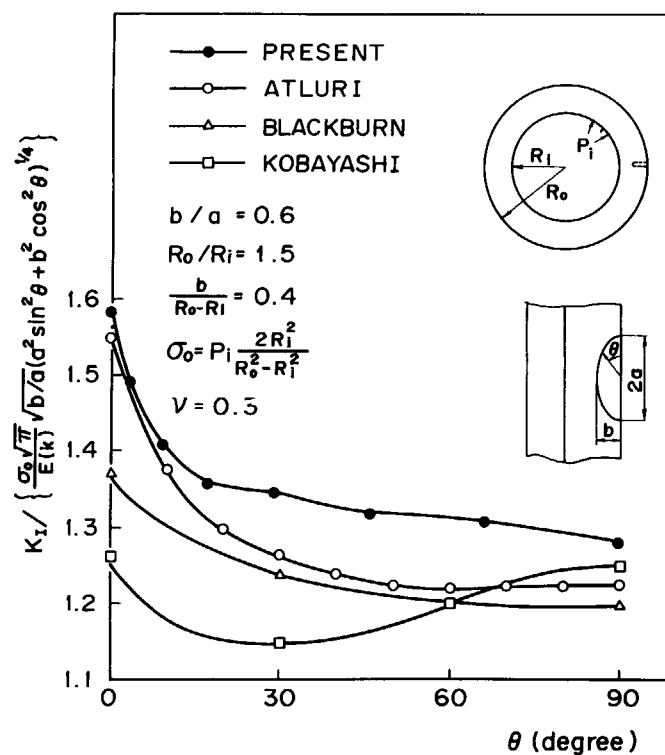

Fig. 3.3.10   Peripheral distribution of nondimensional stress intensity factors for a pressurized cylinder with outer semi-elliptical crack.

$$K_0 = \frac{\sigma_0 \sqrt{\pi}}{E(k)} \sqrt{b/a} \, (a^2 \sin^2\theta + b^2 \cos^2\theta)^{1/4}$$

$E(k)$: Elliptic integral of the second kind

$k^2 = 1 - (b/a)^2$

$$\sigma_0 = \frac{2R_i^2 P_i}{R_0^2 - R_i^2}$$

The results obtained by Atluri and Kathiresan[20], Blackburn and Hellen[21], and Kobayashi, et al.[22] are also given in the figure. Atluri and Kathiresan used the special elements containing the singularity of stress around the crack and the hybrid displacement technique to satisfy the continuity of the displacement between the special and conventional elements. In this method, the stress intensity factors can be solved directly along with the unknown nodal displacements. Blackburn and Hellen utilized the virtual crack extension method. Kobayashi, et al. obtained the stress intensity factor by applying the curvature correction to that of the surface crack in the flat plate. The geometric parameters in Atluri and Kathiresan's and Kobayashi, et al.'s analyses were same as present one, while Balckburn and Hellen analyzed the cylinder with $R_o/R_i = 1.461$. Farily good agreement is found between present and Atluri and Kathiresan's solutions.

3.3.2 Circumferential Circular Shaped Cracks in Inner Surface of a Cylinder Subjected to Shear Force

As in the following paragraphs are shown the analytical results of the stress intensity factors of circumferential circular shaped single crack or three cracks in a cylinder subjected to shear force.

[I] Single Crack Case

Figure 3.3.11 shows the cylinder subjected to shear force P of 17330 kg. Single surface crack was assumed to be contained in the fixed end C–C' in the figure. Following two cases
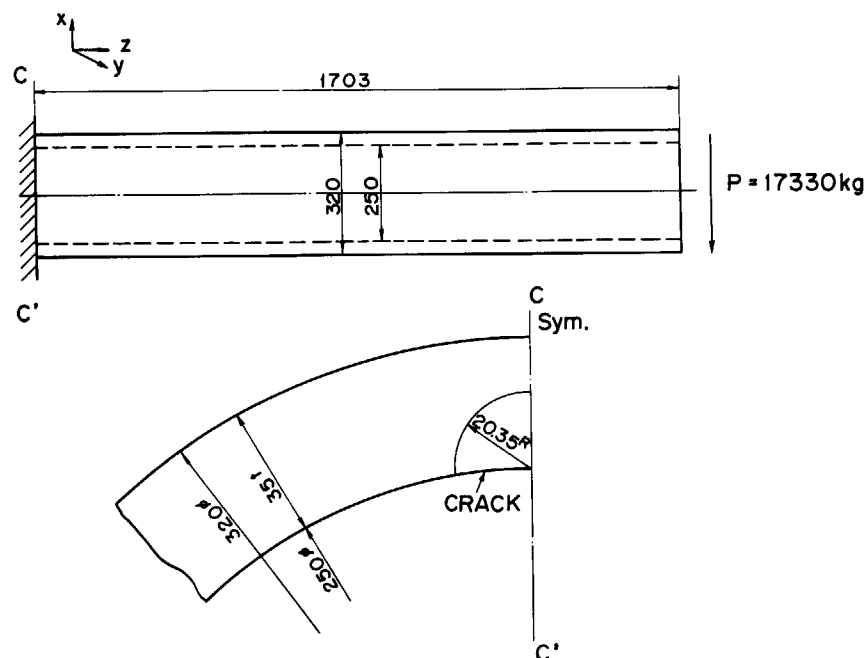

Fig. 3.3.11 A cylinder with a single semi-circular crack subjected to shear force.
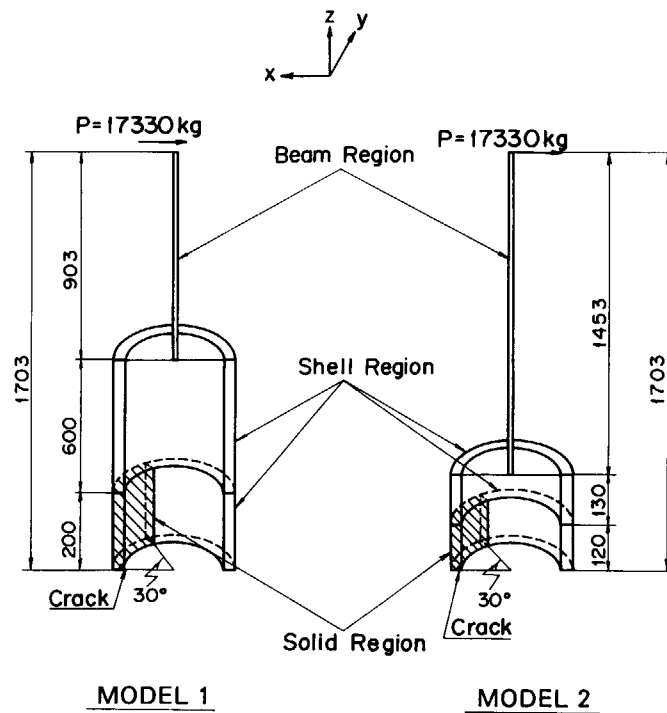
Fig. 3.3.12   Analytical Models of a cylinder with a single semi-circular crack subjected to shear force.

were considered as the boundary conditions.

BC-1 :   The cross section C–C' was completely fixed.

BC-2 :   The deformation in the X–Y plane was not constrained in the fixed end C–C'.

Young's modulus and Poission's ratio were assumed to be 19700 kg/mm² and 0.3, respectively.

As shown in **Fig. 3.3.12**, one half of the cylinder was analyzed due to the symmetry of the structure. The 16-node solid elements (SOLID16) were allocated at the neighborhood of the crack, while the shell and beam elements (FSHEL4 and BEAM3D) were used to model the remainder of the cylinder. The 3-node or 8-node connection elements (BOUND3 or BOUND8) were used to connect the beam and shell elements or the shell and solid elements. The above modeling was employed due to the reasons that the region near the surface crack was governed by the three-dimensional stress field and that the whole deformation of the cylinder could be represented by the beam type simplification. Two models shown in **Fig. 3.3.12** were taken to study the effect of different model of the cylinder on the stress intensity factors. **Figures 3.3.13(a)** and **(b)** show the finite element mesh of the cylinder in the development figure. **Figure 3.3.14** shows the finite element mesh in the surface with the crack which was used in both cases of MODEL 1 and MODEL 2. The distorted elements were allocated along the crack front. The numbers of each element, nodes, and total degrees-of-freedom used in the analyses are shown in **Table 3.3.2**.

Figure 3.3.15 shows the comparison of the axial distributions of deflection U_x for the case of BC-1 between the present analysis and the beam theory. The deflection U_z obtained from the present analysis is found to vary smoothly at the boundary of different kinds of element. It is also found from the figure that the present results are in good agreement with that of the beam theory.

Figure 3.3.16 shows the distributions of deflection U_z along circumferential direction. The boundary of the solid and shell elements are $z = 200$ mm and $\theta = 30°$ for MODEL 1, and z
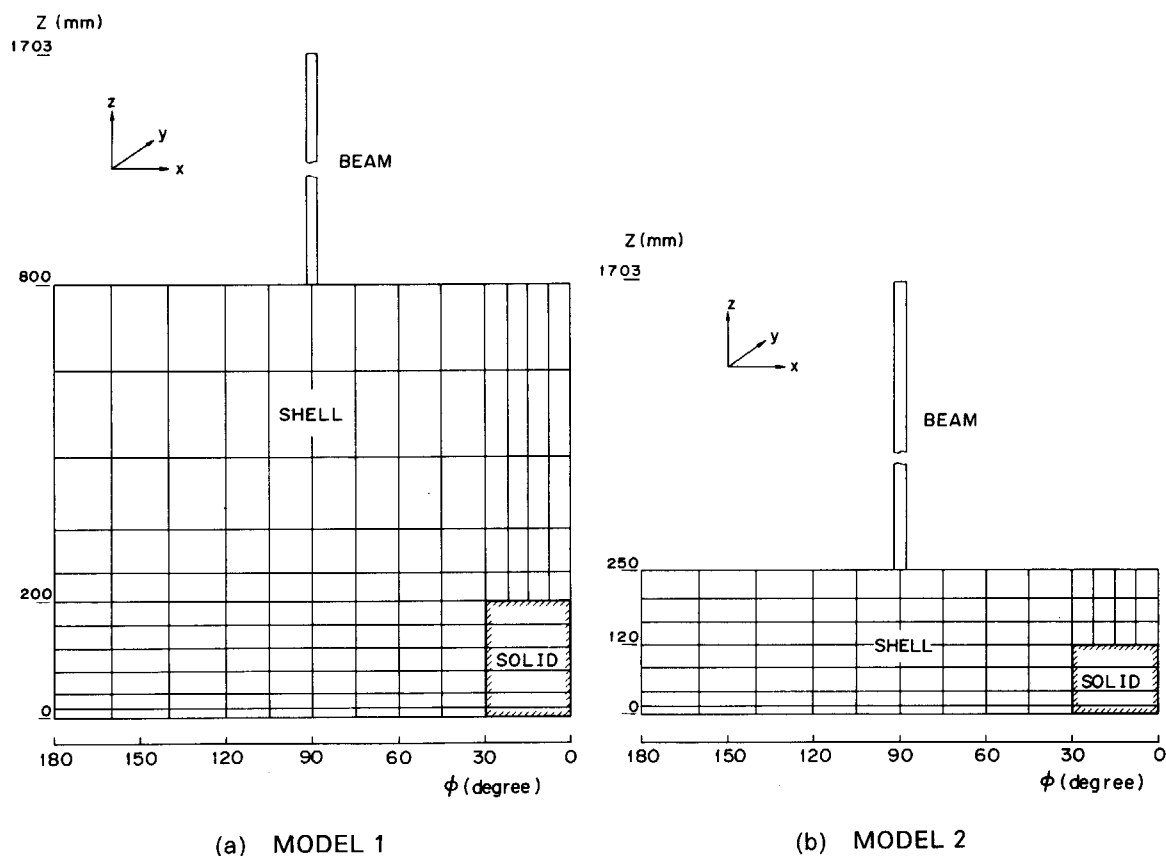
(a) MODEL 1   (b) MODEL 2

Fig. 3.3.13 Finite element mesh of a cylinder with a single semi-circular crack
                 subjected to shear force.

Distorted Elements
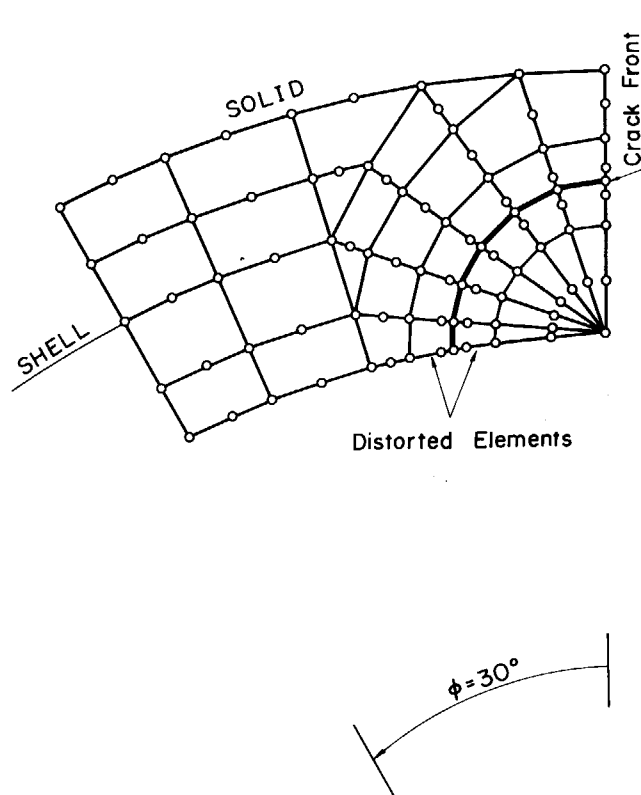
Table 3.3.2 Numbers of elements, nodes
and degrees-of-freedom for the
stress intensity factor analysis
of a cylinder with a single crack
subjected to shear force

	MODEL 1	MODEL 2
Number of Elements		
SOLID16	228	152
FSHEL4	119	75
BEAM3D	6	6
BOUND3	13	13
BOUND8	36	28
Number of Nodes	1,024	714
Number of Degrees-of-freedome	3,597	2,511

$\phi = 30°$

Fig. 3.3.14 Finite element mesh in the surface with crack.

Fig. 3.3.15 Distribution of deflections U_x along z-axis for a cylinder with a single semi-circular crack subjected to shear force.
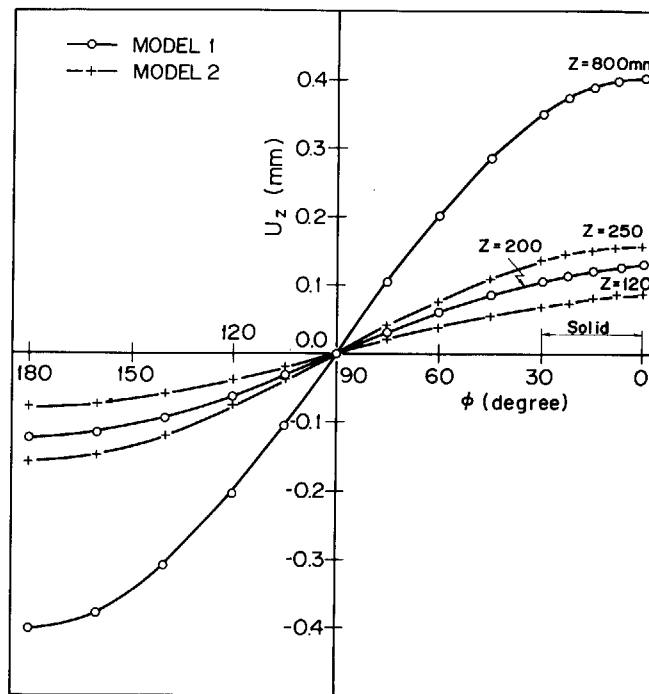
Fig. 3.3.16 Distribution of deflections U_z along circumference for a cylinder with a single semi-circular crack subjected to shear force.
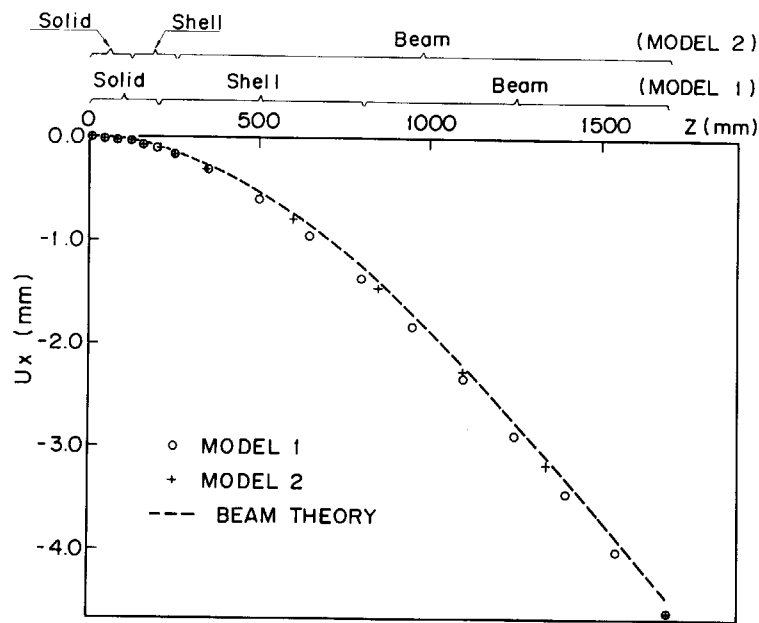
= 120 mm and θ = 30° for MODEL 2. No disturbance of U_z is found at the boundary of the solid and shell elements.

Figure 3.3.17 shows the axial distributions of the stress σ_z for the case of BC-1. The results of the beam theory are also given in the figure. The present results are found to be in good agreement with those of the beam theory except near the fixed end in which three-dimensional effects are important. On the other hand, discontinuity of the stress is found near the connection of the solid and shell elements, i.e. ϕ = 4°, z = 180 mm for MODEL 1 and
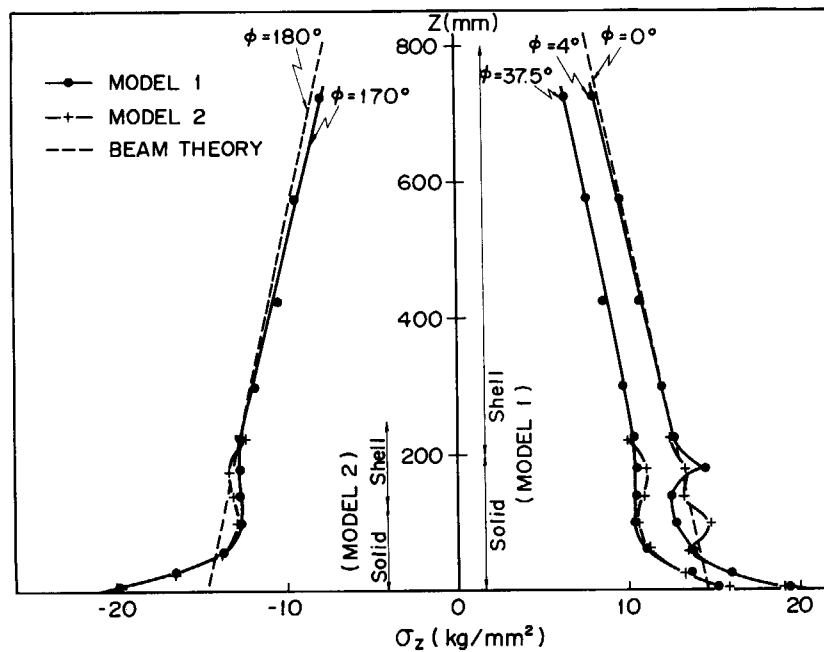
Fig. 3.3.17   Distribution of stresses σ_z along z-axis for a cylinder with a single semi-circular crack subjected to shear force.

$\phi = 4°$, $z = 100$ mm for MODEL 2. This discontinuity is, however, localized and the stress varies smoothly in other part. It is also found that the difference between MODEL 1 and MODEL 2 is very small.

Figures 3.3.18 and **3.3.19** show the peripheral distributions of the stress intensity factors for the case of BC-1 and BC-2, respectively. K_0 in these figures show the stress intensity factor of the circular crack embedded in the infinite body subjected to a uniform stress σ_0

Fig. 3.3.18   Peripheral distribution of stress intensity factors for a cylinder with a single semi-circular crack subjected to shear force — BC-1, Fixed end.

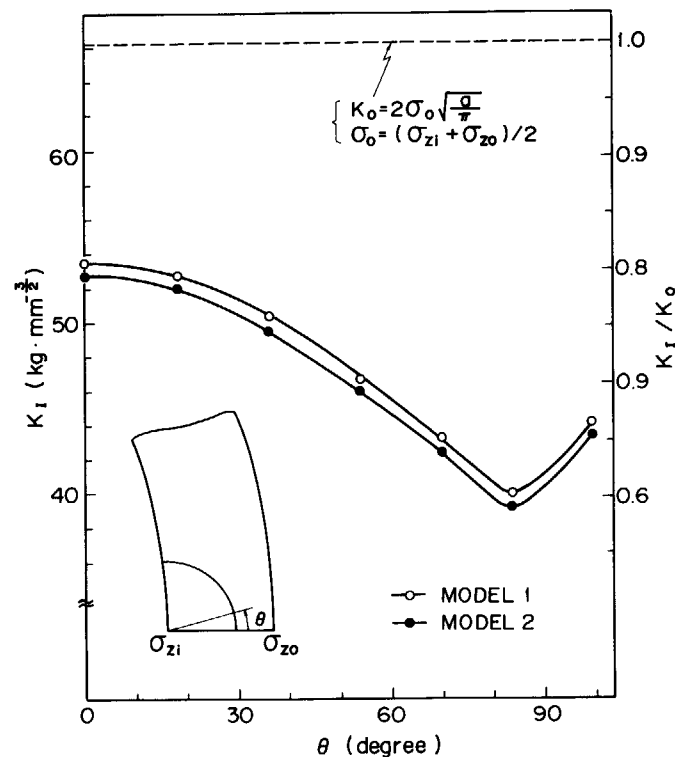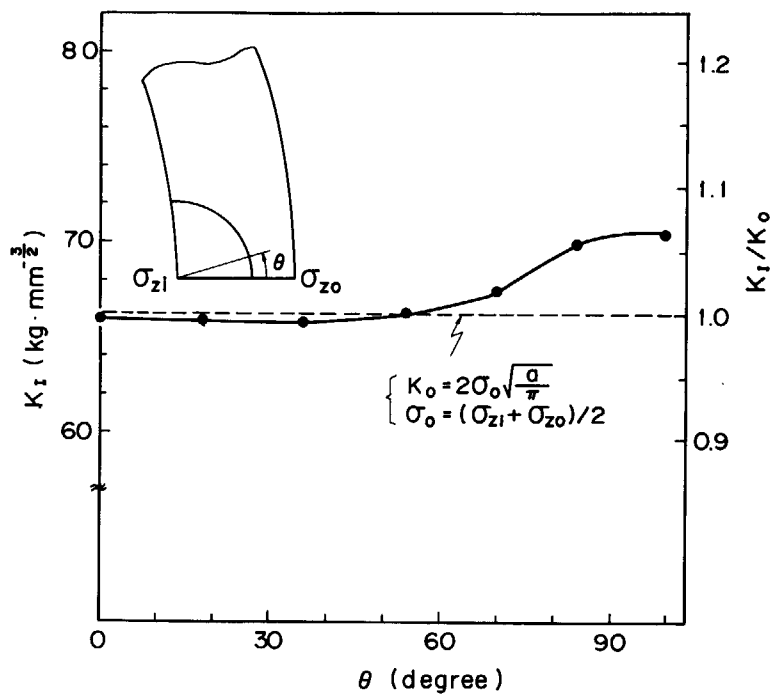**Fig. 3.3.19** Peripheral distribution of stress intensity factors for a cylinder with a single semi-circular crack subjected to shear force — BC-2, Symmetrical end.

corresponding to the average value of σ_{zi} and σ_{zo} which denote the stresses in the inner and outer surface of the cylinder at the cross section C–C' obtained by the beam theory. It is found from **Fig. 3.3.18** that the difference between MODEL 1 and MODEL 2 is less than 2%. This indicates that the accuracy of the stress intensity factor is not deteriorated by the reduction of the solid region such as MODEL 2. Therefore, MODEL 2 was employed to analyze the case of BC-2. It is found from **Fig. 3.3.18** that the stress intensity factor of BC-1 is much smaller than K_0 because of excessive constraint of degrees-of-freedom at the cross section C–C'.

[II] Three Cracks Case

As shown in **Fig. 3.3.20**, three surface cracks were assumed to be contained in the fixed end C–C' of the cylinder shown in **Fig. 3.3.11**. The same loading and material properties as in the single crack case were used in the present analysis. It was assumed that the deformation in
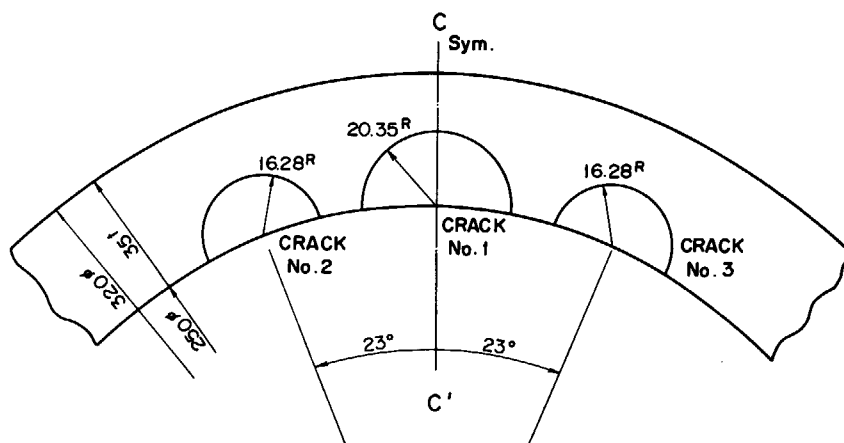
Fig. 3.3.20 A cylinder with three semi-circular cracks subjected to shear force.

the $X-Y$ plane was not constrained in the fixed end C–C′, which was corresponding to BC-2 in the single crack case.

One half of the cylinder was taken due to the symmetry of the structure. The cylinder was modeled by the solid, shell, beam and connection elements (SOLID16, FSHEL4, BEAM3D and BOUND8), as shown in **Fig. 3.3.21**. **Figure 3.3.22** shows the finite element mesh in the development figure. Larger solid element region was taken in this case than in the single crack case previously metioned because of the increase of number of the cracks contained in the fixed end C–C′. **Figure 3.3.23** shows the finite element mesh in the surface with the crack.

Fig. 3.3.21   Analytical model of a cylinder with three semi-circular cracks subjected to shear force force.

Fig. 3.3.22   Finite element mesh of a cylinder with three semi-circular cracks subjected to shear force.

Fig. 3.3.23   Finite element mesh in the surface with cracks.

The distorted elements were allocated along the crack fronts. The same finite element model as the single crack case was us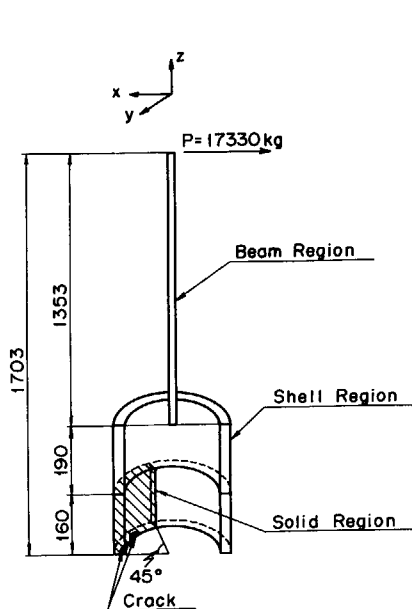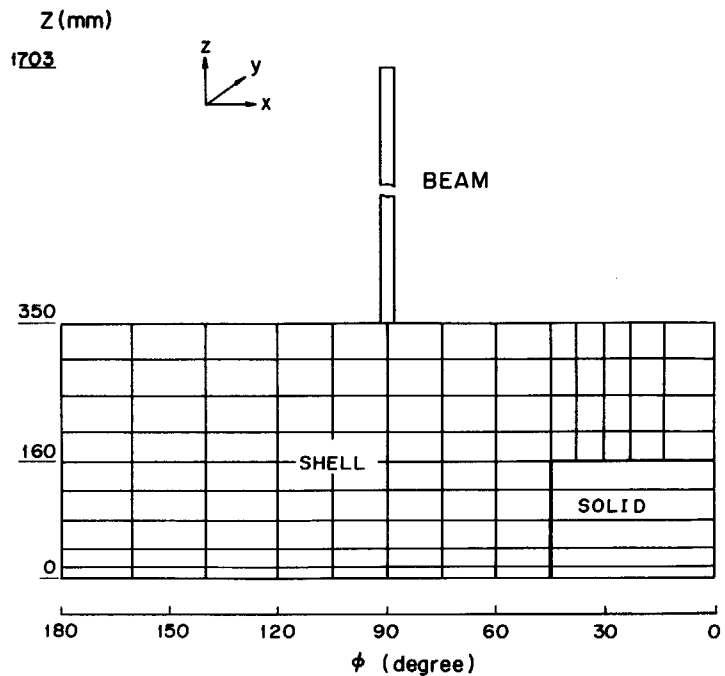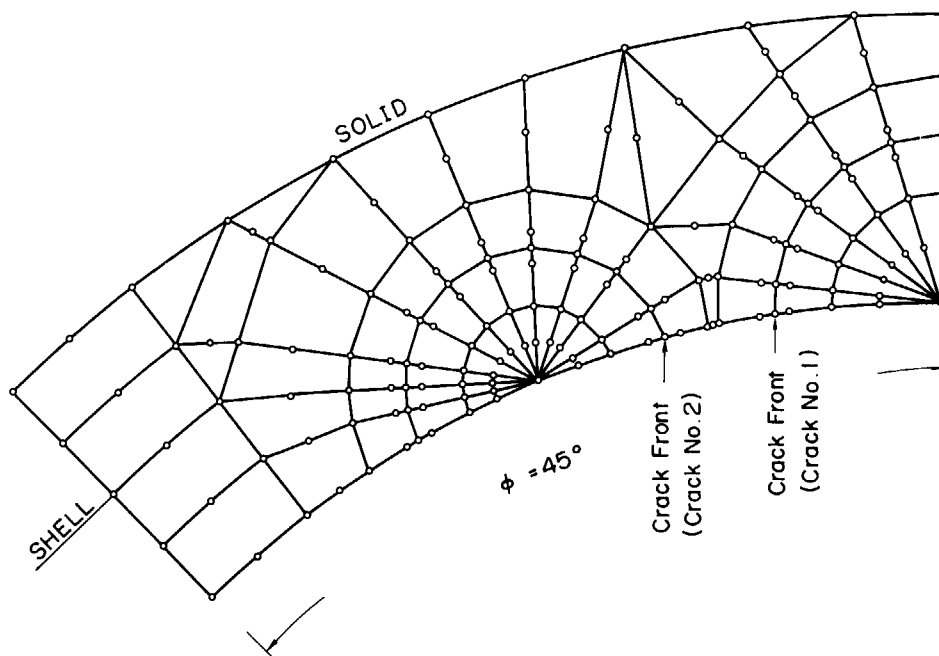ed around Crack No. 1 to obtain the distribution of the stress intensity factor of Crack No. 1 with that of the single crack case obtained in [1] of this section. **Table 3.3.3** shows the numbers of each element, nodes and total degrees-of-freedom used in the analysis.

Figure 3.3.24 shows the peripheral distributions of the stress intensity factor where the result is also given for the single crack which had the same geometry as Crack No. 1 in **Fig. 3.3.20**. It can be seen from the figure that the stress intensity factor of Crack No. 1 is higher by 3 ~ 9% than that of single crack. The difference between the result of Crack No. 1 of the three cracks and that of the single crack is found to become larger in the region of large angle θ where Cracks No. 1 and No. 2 are contiguous to each other. It may be, therefore, concluded that the effect of interaction of the nearly-located surface cracks is found in the stress intensity factor of Crack No. 1.

Table 3.3.3 Numbers of elements, nodes and degrees-of-freedom for the stress intensity factor analysis of a cylinder with three cracks subjected to shear force

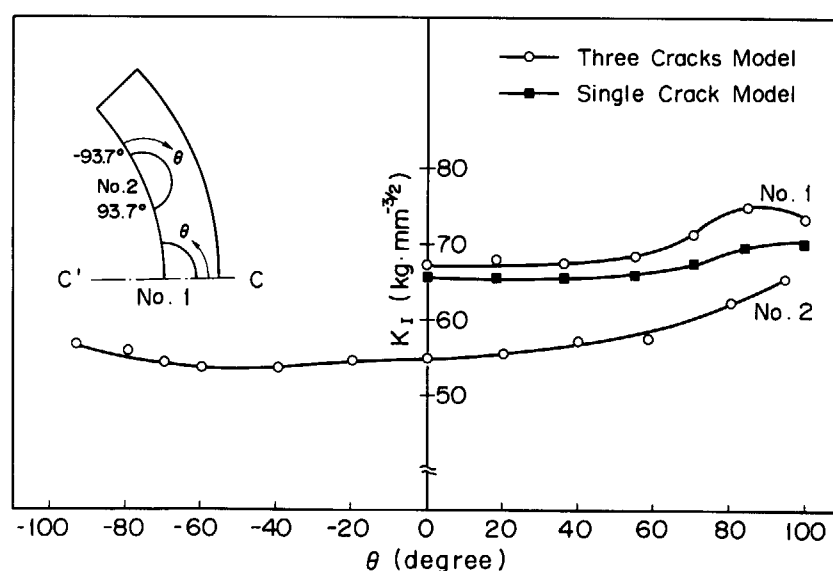| Number of Elements	
SOLID16	385
FSHEL4	92
BEAM3D	6
BOUND8	32
BOUND3	13
Number of Nodes	1,517
Number of Degrees-of-freedom	4,989

Fig. 3.3.24 Peripheral distribution of stress intensity fastors for a cylinder with three semi-circular crack subjected to shear force.

4. Conclusions

Theoretical background and application of the EPAS-J1 program were presented in this paper. The special feature of this program is inclusion of the connection elements based on the Lagrange multiplier concept, by which different kinds of elements can be connected easily. Computer storage and computational time can be reduced meaningfully using different kinds of elements for calculation of the stress intensity factors of the three-dimensional surface cracks. The following conclusions were obtained by the analyses using the EPAS-J1 program.

(1) The connection elements based on the Lagrange multiplier concept provide more accurate results than other techniques of connecting different kinds of elements such as the tying method or the method using the anisotropic plate element.

(2) Convergent stress intensity factors can be obtained by the virtual crack extension method if the virtual crack extension value Δa is less than $10^{-2} \sim 10^{-3} \ell$ where ℓ denotes the side length of the element measured in the direction of crack extension.

(3) In order to obtain the stress intensity factor of the three-dimensional cracks by the virtual crack extension method, the 16-node solid element (SOLID16) should be used rather than the 20-node solid element (SOLID20), in which the discrepancy is found between the stress intensity factors obtained from the corner-nodes and the mid-nodes of the elements.

(4) In the stress intensity factor analysis of the longitudinal semi-elliptical crack in the outer surface of a pressurized cylinder, fairly good agreement is found between Atluri and Kathiresan's solution and the present one obtained using the modeling of different kinds of elements together with the connection elements.

(5) Comparing the stress intensity factors of circumferential circular shaped single surface crack and nearly-located three surface cracks in the inner surface of a cylinder subjected to shear force, interaction effect of multiple surface cracks is found in the stress intensity factors.

Acknowledgements

References

1) Reynen J.: On the Use of Finite Elements in Fracture Analysis of Pressure Vessel Component, J. Pressure Vessel Technology, Trans. ASME Ser. J, Vol. 98, No. 1, pp. 8–16 (1976).

2) Broekhoven M.J.G.: Computation of Stress Intensity Factors for Nozzle Corner Cracks by Various Finite Element Procedures, "3rd Conf. Struct. Mech. in Reactor Tech", G 4/6 (1975).

3) Hall C.A., Raymund M. and Palusamy S.: A Macro Element Approach to Computing Stress Intensity Factors for Three Dimensional Structures, Int. J. Fracture, Vol. 15, No. 3, pp. 231–245 (1979).

4) Bergan P.G. and Aamodt B.: Finite Element Analysis of Crack Propagation in Three-Dimensional Solid under Cyclic Loading, "2nd Conf. Struct. Mech. in Reactor Tech", G 5/5 (1973).

5) Yagawa G., Watanabe T., Ishiwata T. and Ando Y.: EPAS-Finite Element Program for Analysis of Nonlinear Behavior of Nuclear Power Piping, "5th Conf. Struct. Mech. in Reactor Tech", M 6/4 (1979).

6) Gallagher R.H.: A Review of Finite Element Techniques in Fracture Mechanics, "Proceeding of the 1st Int. Conf. on Num. Meth. in Fract. Mech", pp. 1–25 (1978).

7) Parks D.M.: A Stiffness Derivative Finite Element Technique for Determination of Elastic Crack Tip Stress Intensity Factors, Int. J. Fract., Vol. 10, pp. 485–502 (1974).

8) Hellen T.K.: On the Method of Virtual Crack Extensions, Int. J. Num. Meth. Engng., Vol. 9, pp. 187–207 (1975).

9) Henshell R.D. and Shaw K.G.: Crack Tip Finite Elements are Unnecessary, Int. J. Num. Meth. Engng, Vol. 9, pp. 495–507 (1975).

10) Barsoum R.S.: On the use of Isoparametric Finite Elements in Linear Fracture Mecharics, Int. J. Num. Meth. Engng. Vol. 10, pp. 25–37 (1976).

11) Hibbitt H.D.: Some Properties of Singular Isoparametric Elements, Int. J. Num. Meth. Engng., Vol. 11, pp. 180–184 (1977).

12) Washizu, K., "Variational Method in Elasticity and Plasticity", 2nd ed., Pergamon Press (1975).

13) Zienkiewicz O.C.: "The Finite Element Method", 3rd ed. McGraw-Hill (1977).

14) Watwood Jr. V.B.: The Finite Element Method for Prediction of Crack Behavior, Nucl. Engng. & Design, Vol. 11, pp. 323–332 (1969).

15) Report on Research Cooperation Sub-Committee 46 on Research and Development of Methods for Inelastic Structural Analysis (II), JSME, pp. 349–357, 537–545 (1979).

16) Ishida M.: Effect of Width and Length on Stress Intensity Factors of Internally Cracked Plates Under Various Boundary Conditions, Int. J. Fract. Mech., Vol. 7, pp. 301–316 (1971).

17) Yagawa G., Ichimiya M. and Ando Y.: An Analysis Method of Stress Intensity Factors Based on Deiscretization Error in Finite Element Technique, Trans. JSME, Vol. 44, No. 379, pp. 743–755 (1978).

18) Tracey D.M.: Finite Elements for Three-Dimensional Elastic Crack Analysis, Nucl. Engng. & Design, Vol. 26, pp. 282–290 (1974).

19) Yagawa G., Ichimiya M. and Ando Y.: Two and Three-Dimensional Analysis of Stress

Intensity Factors Based on Discretization Error in Finite Elements, "Proceedings of the 1st Int. Conf. on Num. Meth. in Fract. Mech.", pp. 249–267 (1978).

20) Atluri S.N. and Kathiresan K.: 3D Analysis of Surface Flaws in Thick-Walled Reactor Pressure-Vessels Using Displacement-Hybrid Finite Element Method., Nucl. Engng. & Design, Vol. 51, pp. 163–176 (1979).

21) Blackburn W.S. and Hellen T.K.: Calculation of Stress Intensity Factors for Elliptical and Semi-Elliptical Cracks in Blocks and Cylinders, Central Electricity Generating Board Report No. RD/B/N 3103 (1974).

22) Kobayashi A.S., Polvnicha N., Emery A.F. and Love W.J.: Inner and Outer Cracks in Internally Pressurized Cylinders, J. Pressure Vessel Technology, Tans. ASME Ser. J, Vol. 99, No. 1, pp. 83–89 (1977).

Nomenclature

A	= crack area
B_{ijk}	= component of transformation matrix between strain and displacement
$E^e_{ijk\ell}$	= elastic modulus
f	= yield function
G	= energy release rate
$[I]$	= unit matrix
$[J]$	= Jacobian matrix
K_I, K_{II}, K_{III}	= stress intensity factors corresponding to Mode I, II and III
n_j	= unit normal vector outwards on S
$\bar{P}_i$	= body force
q_j	= nodal displacement
r_j	= generalized coordinate of fictitious element
S_u	= displacement boundary
S_σ	= mechanical boundary
$S^{(12)}$	= fictitious boundary surface
T	= temperature
T_i	= traction force
u_i	= displacement
V	= region of continuum
X_i	= coordinate
σ_{ij}	= stress
ϵ_{ij}	= strain
λ_i	= Lagrange multiplier
θ_i	= rotation
$\phi_{ij}, \psi_{ij}, \Omega_{ij}$	= interpolation functions
$(\bar{})$	= prescribed value
$\Delta()$	= incremental value
$()^e$	= elastic component
$()^p$	= plastic component
$()^{ep}$	= elastic-plastic component
$()^\theta$	= thermal component
$()^{(\alpha)}$	= quantity belonging to fictitious region
$\delta()$	= virtual quantity
$\{\}$	= vector
$[]$	= matrix
$[]^t$	= transpose matrix
$[]^{-1}$	= inverse matrix
$()_{,i}$	= partial differentiation with respect to coordinate i

Appendix A. Constitutive Equation for Thermo-elastoplasticity

Here is shown the derivation of the constitutive equation for thermo-elastic-plastic behavior of materials.

The stress-strain relation is generally given as follows:

$$\sigma_{ij} = E^e_{ijk\ell}\, \epsilon^e_{k\ell} \tag{A.1}$$

in which σ_{ij}, ϵ^e_{ij} and $E^e_{ijk\ell}$ represent the stress, the elastic strain and the elastic modulus, respectively. Assuming that $E^e_{ijk\ell}$ is a function of temperature T, the incremental form of eq. (A.1) is given as follows:

$$d\sigma_{ij} = E^e_{ijk\ell}\, d\epsilon^e_{k\ell} + \frac{\partial E^e_{ijk\ell}}{\partial T}\, \epsilon^e_{k\ell}\, dT \tag{A.2}$$

The plastic strain increment is written as follows using the incremental theory of plasticity:

$$d\epsilon^p_{ij} = d\lambda \frac{\partial \phi}{\partial \sigma_{ij}} \tag{A.3}$$

where ϕ and positive value $d\lambda$ denote the plastic potential and the unknown constant. Let us assume that the yield suface is given as follows:

$$f(\sigma_{ij}, \epsilon^p_{ij}, T) = 0 \tag{A.4}$$

According to the associated flow rule, the above function f is used as the plastic potential. Then, eq. (A.3) yields

$$d\epsilon^p_{ij} = d\lambda \frac{\partial f}{\partial \sigma_{ij}} \tag{A.5}$$

Furthermore, it is assumed that the incremental strain $\Delta\epsilon_{ij}$ can be decomposed as follows:

$$d\epsilon_{ij} = d\epsilon^e_{ij} + d\epsilon^p_{ij} + d\epsilon^\theta_{ij} + d\epsilon^c_{ij} + d\epsilon^s_{ij} \tag{A.6}$$

$d\epsilon^\theta_{ij}$, $d\epsilon^c_{ij}$ and $d\epsilon^s_{ij}$ in eq. (A.6) are the increments of thermal strain, creep strain and swelling strain, respectively, and these components are written as follows:

$$d\epsilon^\theta_{ij} = \delta_{ij}\alpha dT$$

$$d\epsilon^c_{ij} = d\bar{\epsilon}^c\, \frac{\partial f}{\partial \sigma_{ij}}$$

$$d\epsilon^s_{ij} = \delta_{ij} dV$$

in which α, δ_{ij}, dV and $d\bar{\epsilon}^c$ denote the thermal expansion coefficient, the Croneker's delta, the increment of average volume and the increment of equivalent creep strain, respectively. $d\epsilon^{ep}_{ij}$ is defined by the sum of $d\epsilon^e_{ij}$ and $d\epsilon^p_{ij}$ as follows:

$$d\epsilon^{ep}_{ij} = d\epsilon^e_{ij} + d\epsilon^p_{ij} = d\epsilon_{ij} - d\epsilon^\theta_{ij} - d\epsilon^c_{ij} - d\epsilon^s_{ij} \tag{A.7}$$

The increment of eq. (A.4) are given as follows:

$$df = \frac{\partial f}{\partial \sigma_{ij}} d\sigma_{ij} + \frac{\partial f}{\partial \epsilon^p_{ij}} d\epsilon^p_{ij} + \frac{\partial f}{\partial T} dT = 0 \tag{A.8}$$

By using eq. (A.7), eq. (A.2) becomes as follows:

$$d\sigma_{ij} = E^e_{ijk\ell}(d\epsilon^{ep}_{k\ell} - d\epsilon^p_{k\ell}) + \frac{\partial E^e_{ijk\ell}}{\partial T} \epsilon^e_{k\ell} dT \tag{A.9}$$

Substituting eq. (A.5) into eqs. (A.8) and (A.9) yields

$$df = \frac{\partial f}{\partial \sigma_{ij}} d\sigma_{ij} + \frac{\partial f}{\partial \epsilon^p_{ij}} \frac{\partial f}{\partial \sigma_{ij}} d\lambda + \frac{\partial f}{\partial T} dT = 0 \tag{A.10}$$

$$d\sigma_{ij} = E^e_{ijk\ell}\left(d\epsilon^{ep}_{k\ell} - d\lambda\frac{\partial f}{\partial \sigma_{k\ell}}\right) + \frac{\partial E^e_{ijk\ell}}{\partial T} \epsilon^e_{k\ell} dT \tag{A.11}$$

$d\lambda$ can be obtained by eliminating $d\sigma_{ij}$ from eqs. (A.10) and (A.11) as follows:

$$d\lambda = \frac{\dfrac{\partial f}{\partial \sigma_{ij}} E^e_{ijk\ell} d\epsilon^{ep}_{k\ell} + \dfrac{\partial f}{\partial \sigma_{ij}} \dfrac{\partial E^e_{ijk\ell}}{\partial T} \epsilon^e_{k\ell} dT + \dfrac{\partial f}{\partial T} dT}{-\dfrac{\partial f}{\partial \epsilon^p_{ij}} \dfrac{\partial f}{\partial \sigma_{ij}} + \dfrac{\partial f}{\partial \sigma_{ij}} E^e_{ijk\ell} \dfrac{\partial f}{\partial \sigma_{k\ell}}} \tag{A.12}$$

The following stress-strain relation can be obtained by substituting eq. (A.12) into eq. (A.11):

$$d\sigma_{ij} = \left(E^e_{ijk\ell} - \frac{E^e_{ijmn} \dfrac{\partial f}{\partial \sigma_{mn}} \dfrac{\partial f}{\partial \sigma_{op}} E^e_{opk\ell}}{-\dfrac{\partial f}{\partial \epsilon^p_{mn}} \dfrac{\partial f}{\partial \sigma_{mn}} + \dfrac{\partial f}{\partial \sigma_{mn}} E^e_{mnop} \dfrac{\partial f}{\partial \sigma_{op}}}\right) d\epsilon^{ep}_{k\ell}$$

$$+ \left(\frac{\partial E^e_{ijk\ell}}{\partial T} \epsilon^e_{k\ell} - \frac{E^e_{ijk\ell} \dfrac{\partial f}{\partial \sigma_{k\ell}}\left(\dfrac{\partial f}{\partial \sigma_{mn}} \dfrac{\partial E^e_{mnop}}{\partial T} \epsilon^e_{op} + \dfrac{\partial f}{\partial T}\right)}{-\dfrac{\partial f}{\partial \sigma^p_{mn}} \dfrac{\partial f}{\partial \sigma_{mn}} + \dfrac{\partial f}{\partial \sigma_{mn}} E^e_{mnop} \dfrac{\partial f}{\partial \sigma_{op}}}\right) dT$$

$$= E^{ep}_{ijk\ell} d\epsilon^{ep}_{k\ell} + G^{ep}_{ij} dT \tag{A.13}$$

Appendix B. Finite Elements Contained in the EPAS-JI Program

The following elements are contained in the EPAS-J1 program.

ELEMENT NAME	ELEMENT TYPE	No. of Nodes
1. FLA	1D TRUSS ELEMENT	2
2. BEAM2D	2D BEAM ELEMENT	2
3. BEAM3D	3D BEAM ELEMENT	2
4. PLANE4	2D PLANE STRESS ELEMENT	4
5. PLANE8	2D PLANE STRESS ELEMENT	8
6. STRAN4	2D PLANE STRAIN ELEMENT	4
7. STRAN8	2D PLANE STRAIN ELEMENT	8
8. SRING4	2D AXISYMMETRIC ELEMENT	4
9. SRING8	2D AXISYMMETRIC ELEMENT	8
10. FSHEL3	3D FLAT SHELL ELEMENT	3
11. FSHEL4	3D FLAT SHELL ELEMENT	4
12. TSHEL8	3D CURVED THICK SHELL ELEMENT	8
13. SOLID8	3D SOLID ELEMENT	8
14. SOLID16	3D SOLID ELEMENT	16
15. SOLID20	3D SOLID ELEMENT	20
16. BOUND3	FSHEL4-BEAM3D CONNECTION ELEMENT	3
17. BOUND8	SOLID16-FSHEL4 CONNECTION ELEMENT	8
18. BOUND10	SOLID20-FSHEL4 CONNECTION ELEMENT	10

Appendix C. Application of Virtual Crack Extension Method to Mixed Mode Stress Intensity Factor Analysis of Two-dimensional Crack

Ishikawa[C.1] proposed the method for obtaining the mixed mode stress intensity factor based on the path independent J integral. Here, the virtual crack extension method is extended to the mixed mode stress intensity factor analysis of the two-dimensional crack.

The potential energy of the total structure π can be written as follows:

$$\pi = \sum_{i=1}^{NT} \int_{V_i} W dV_i - U^T F(X) = \sum_{i=1}^{NT} \hat{W}_i (U, X) - U^T F(X) \tag{C.1}$$

in which

W = strain energy density

V_i = volume of the i-th element of the mesh

U = vector of nodal displacement.

F = nodal force vector

X = vector of nodal coordinate

$\hat{W}_i$ = integral of strain energy density

NT = total number of elements

$(\ )^T$ = transpose of matrix or vector

The increment of potential energy $\delta\pi$ can be given as follows:

$$\delta\pi = \delta U^T \frac{\partial\pi}{\partial U} + \partial X^T \frac{\partial\pi}{\partial X}$$

$$= \delta U^T \cdot \left[\sum_{i=1}^{NT} \frac{\partial\hat{W}_i}{\partial U} - F(X) \right] + \delta X^T \cdot \left[\sum_{i=1}^{NT} \frac{\partial\hat{W}_i}{\partial X} - \frac{\partial F^T}{\partial X} \cdot U \right] \tag{C.2}$$

The first term in eq. (C.2) is equal to zero due to the equilibrium condition. Then, eq. (C.2) yields as follows:

$$\delta\pi = \delta X^T \cdot \left[\sum_{i=1}^{NT} \frac{\partial\hat{W}_i}{\partial X} - \frac{\partial F^T}{\partial X} \cdot U \right] \tag{C.3}$$

Now consider the virtual crack extension of the two dimensional crack shown in **Fig. C.1**. In the figure, Γ_1 is fixed and the x-coordinates of all nodes on and within an interior Γ_0 which surrounds the crack tip are incremented virtually by the amount of $\delta\ell$. Then, the virtual variation of the potential energy can be written as follows:

$$\frac{\delta\pi}{\delta\ell} = \sum_{i=1}^{NT} \frac{\partial\hat{W}_i}{\partial X} - \frac{\partial F^T}{\partial X} \cdot U \tag{C.4}$$

For the two-dimensional elasticity, the integral of the strain energy density $\hat{W}_i$ is represented as follows:

$$\hat{W}_i = \int_{V_i} w dV_i = t \int_{A_i} W dA \tag{C.5}$$

in which t and A denote the plate thickness and the area of the i-th element of the mesh, respectively. On the other hand, W in eq. (C.5) is given as follows.

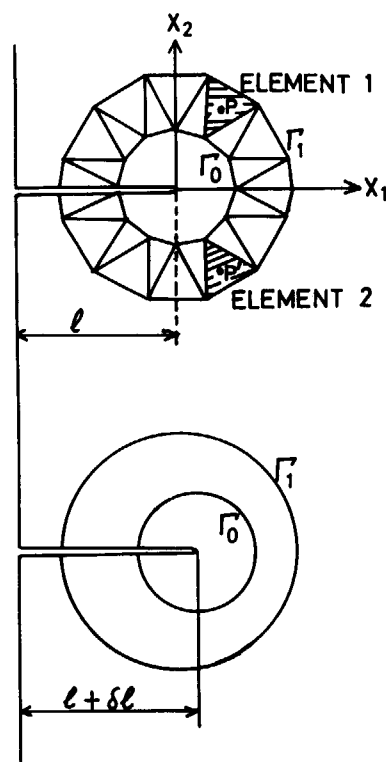$$W = \int_0^{\epsilon_{ij}} \sigma_{ij} d\epsilon_{ij} \tag{C.6}$$

Fig. C.1.   Virtual Crack Extension for Mixed Mode Crack.

Two points P and P' shown in **Fig. C.1** are symmetric with respect to the x_1-axis. The stresses and displacements of the point P are separated into the sum of Mode I and Mode II components using those of the points P and P' as follows:

$$\cdot \quad \sigma_{ij} = \sigma_{ij}^I + \sigma_{ij}^{II} \tag{C.7}$$

$$\begin{Bmatrix} \sigma_{11}^I \\ \sigma_{22}^I \\ \sigma_{12}^I \end{Bmatrix} = \frac{1}{2} \begin{Bmatrix} \sigma_{11} + \sigma_{11}' \\ \sigma_{22} + \sigma_{22}' \\ \sigma_{12} - \sigma_{12}' \end{Bmatrix}, \qquad \begin{Bmatrix} \sigma_{11}^{II} \\ \sigma_{22}^{II} \\ \sigma_{12}^{II} \end{Bmatrix} = \frac{1}{2} \begin{Bmatrix} \sigma_{11} - \sigma_{11}' \\ \sigma_{22} - \sigma_{22}' \\ \sigma_{12} + \sigma_{12}' \end{Bmatrix} \tag{C.7'}$$

$$\cdot \quad U_i = U_i^I + U_i^{II} \tag{C.8}$$

$$\begin{Bmatrix} U_1^I \\ U_2^I \end{Bmatrix} = \frac{1}{2} \begin{Bmatrix} U_1 + U_1' \\ U_2 + U_2' \end{Bmatrix}, \qquad \begin{Bmatrix} U_1^{II} \\ U_2^{II} \end{Bmatrix} = \frac{1}{2} \begin{Bmatrix} U_1 - U_1' \\ U_2 + U_2' \end{Bmatrix} \tag{C.8'}$$

where the superscripts I and II denote the values pertinent to Mode I and Mode II, and the superscript ( )' represents the value of the point P'. Using the strain-displacement relation

$$\epsilon_{ij}^M = \frac{1}{2} (U_{i,j}^M + U_{j,i}^M) \quad (M = I, II) \tag{C.9}$$

together with eq. (C.8), the strains of the point P are also separated into the same form as eqs. (C.7) and (C.7') as follows:

$$\cdot \quad \epsilon_{ij} = \epsilon_{ij}^I + \epsilon_{ij}^{II} \tag{C.10}$$

$$
\left\{ \begin{array}{c} \epsilon_{11}^{I} \\ \epsilon_{22}^{I} \\ \epsilon_{12}^{I} \end{array} \right\} = \frac{1}{2} \left\{ \begin{array}{c} \epsilon_{11} + \epsilon_{11}' \\ \epsilon_{22} + \epsilon_{22}' \\ \epsilon_{12} - \epsilon_{12}' \end{array} \right\}, \qquad \left\{ \begin{array}{c} \epsilon_{11}^{II} \\ \epsilon_{22}^{II} \\ \epsilon_{12}^{II} \end{array} \right\} = \frac{1}{2} \left\{ \begin{array}{c} \epsilon_{11} - \epsilon_{11}' \\ \epsilon_{22} - \epsilon_{22}' \\ \epsilon_{12} + \epsilon_{12}' \end{array} \right\} \qquad (C.10')
$$

Using eqs. (C.5), (C.6), (C.7) and (C.10), the following equation can be obtained:

$$
\hat{W}_i = \frac{t}{2} \int_{A_i} \left(\int_0^{\epsilon_{ij}} \sigma_{ij} \, d\epsilon_{ij} \right) dA
$$

$$
= \frac{t}{2} \int_{A_i} \left(\int_0^{\epsilon_{ij}} (\sigma_{ij}^{I} + \sigma_{ij}^{II}) \, d(\epsilon_{ij}^{I} + \epsilon_{ij}^{II}) \right) dA
$$

$$
= (\hat{W}_{II} + \hat{W}_{IIII} + \hat{W}_{III} + \hat{W}_{III}) \qquad (C.11)
$$

in which

$$
\hat{W}_{MN} = \frac{t}{2} \int_{A_i} (\sigma_{ij}^{M} \, d\epsilon_{ij}^{N}) \, dA \quad (M, N = I, II) \qquad (C.12)
$$

Let us consider the hatched two elements, Element 1 and Element 2, shown in **Fig. C.1** which are symmetric with respect to x_1-axis. The following relations can be obtained in the two elements using eqs. (C.7) and (C.10).

$$
\left\{ \begin{array}{l} \sigma_{11}^{I}{}' = \sigma_{11}^{I} \\ \sigma_{22}^{I}{}' = \sigma_{22}^{I} \\ \sigma_{12}^{I}{}' = -\sigma_{12}^{I} \end{array} \right. \qquad \left\{ \begin{array}{l} \epsilon_{11}^{I}{}' = \epsilon_{11}^{I} \\ \sigma_{22}^{I}{}' = \epsilon_{22}^{I} \\ \epsilon_{12}^{I}{}' = -\epsilon_{12}^{I} \end{array} \right. \qquad (C.13)
$$

$$
\left\{ \begin{array}{l} \sigma_{11}^{II}{}' = -\sigma_{11}^{II} \\ \sigma_{22}^{II}{}' = -\sigma_{22}^{II} \\ \sigma_{12}^{II}{}' = \sigma_{12}^{II} \end{array} \right. \qquad \left\{ \begin{array}{l} \epsilon_{11}^{II}{}' = -\epsilon_{11}^{II} \\ \epsilon_{22}^{II}{}' = -\epsilon_{22}^{II} \\ \epsilon_{12}^{II}{}' = \epsilon_{12}^{II} \end{array} \right. \qquad (c.14)
$$

Introducing eqs. (C.13) and (C.14) into eq. (C.12) leads to the following relations.

$$
\left\{ \begin{array}{l} \hat{W}_{II}' = \hat{W}_{II} \\ \hat{W}_{III}' = -\hat{W}_{III} \end{array} \right. \qquad \left\{ \begin{array}{l} \hat{W}_{IIII}' = \hat{W}_{IIII} \\ \hat{W}_{III}' = -\hat{W}_{III} \end{array} \right. \qquad (C.15)
$$

In eqs. (C.13) through (C.15), the notaions with and without the superscript " ' " represent the values pertinent to Element 2 and Element 1, respectively.

Let us assume that the number of the element surrounded between Γ_0 and Γ_1 are $2N$, among which N elements are contained in the plus region of x_2, and other N elements exist in the minus region of x_2, and that finite element mesh is symmetric with respect to the x_1-axis. The following relation is obtained, considering that only the elements surrounded between Γ_0 and Γ_1 are subjected to the variation of strain energy due to the virtual crack extension and using the relations given in eq. (C.15):

$$
\sum_{i=1}^{NT} \frac{\partial \hat{W}_i}{\partial X} = \sum_{i=1}^{2N} \frac{\partial \hat{W}_i}{\partial X} = 2 \sum_{i=1}^{N} \left\{ \frac{\partial (\hat{W}_{II})_i}{\partial X} + \frac{\partial (\hat{W}_{IIII})_i}{\partial X} \right\} \qquad (C.16)
$$

For the linear or nonlinear elastic body, the integral of the strain energy density of the i-th element W_i can be also given using the stiffness matrix of i-th element as follows:

$$\hat{W}_i = \frac{1}{2} U^T \cdot K_i \cdot U \tag{C.17}$$

Substituting eq. (C.8) into eq. (C.17) yields the following equation:

$$\hat{W}_i = \frac{1}{2} [(U^I)^T \cdot K_i \cdot (U^I) + (U^{II})^T \cdot K_i \cdot (U^{II})$$

$$+ (U^I)^T \cdot K_i \cdot (U^{II}) + (U^{II})^T \cdot K_i \cdot (U^I)] \tag{C.18}$$

Comparing eq. (C.11) with eq. (C.18), the following equations can be obtained:

$$\begin{cases} (\hat{W}_{I\,I})_i = \frac{1}{2} (U^I)^T \cdot K_i \cdot (U^I) \\ (\hat{W}_{II\,II})_i = \frac{1}{2} (U^{II})^T \cdot K_i \cdot (U^{II}) \end{cases} \tag{C.19}$$

Introducing eq. (C.19) into eq. (C.18) leads to the following equation:

$$\sum_{i=1}^{NT} \frac{\partial \hat{W}_i}{\partial X} = 2 \sum_{i=1}^{N} \left[\frac{1}{2} (U^I)^T \cdot \frac{\partial K_i}{\partial X} \cdot (U^I) + \frac{1}{2} (U^{II})^T \cdot \frac{\partial K_i}{\partial X} \cdot (U^{II}) \right]$$

$$= \sum_{i=1}^{N} \left[(U^I)^T \cdot \frac{\partial K_i}{\partial X} \cdot (U^I) + (U^{II})^T \cdot \frac{\partial K_i}{\partial X} \cdot (U^{II}) \right] \tag{C.20}$$

The second term in the right hand side of eq. (C.4) becomes as follows, using eq. (C.8):

$$\frac{\partial F^T}{\partial X} \cdot U = \frac{\partial F^T}{\partial X} \cdot (U^I + U^{II}) \tag{C.21}$$

Substituting eqs. (C.20) and (C.21) into eq. (C.4), the following equation can be obtained:

$$\frac{\delta \pi}{\delta \ell} = \left[\sum_{i=1}^{N} (U^I)^T \cdot \frac{\partial K_i}{\partial X} \cdot (U^I) - \frac{\partial F^T}{\partial X} \cdot U^I \right]$$

$$+ \left[\sum_{i=1}^{N} (U^{II})^T \cdot \frac{\partial K_i}{\partial X} \cdot (U^{II}) - \frac{\partial F^T}{\partial X} \cdot U^{II} \right] \tag{C.22}$$

Then, the energy release rate G_I and G_{II} corresponding to Mode I and Mode II are given as follows:

$$G_I = \frac{\partial F^T}{\partial X} \cdot U^I - \sum_{i=1}^{N} (U^I)^T \cdot \frac{\partial K_i}{\partial X} \cdot (U^I)$$

$$G_{II} = \frac{\partial F^T}{\partial X} \cdot U^{II} - \sum_{i=1}^{N} (U^{II})^T \cdot \frac{\partial K_i}{\partial X} \cdot (U^{II}) \tag{C.23}$$

For the linear elastic body, the stress intensity factor K_I and K_{II} corresponding Mode I and Mode II are related to G_I and G_{II} as follows:

① Plane strain

$$K_I = \left(\frac{E}{1 - \nu^2} G_I \right)^{1/2}, \qquad K_{II} = \left(\frac{E}{1 - \nu^2} G_{II} \right)^{1/2} \tag{C.24}$$

② Plane stress

$$K_I = (E \, G_I)^{1/2}, \qquad K_{II} = (E G_{II})^{1/2} \tag{C.25}$$

in which E and ν denote the modulus of elasticity and Poission's ratio, respectively.

The description presented here is based on the private communication[C.2] of one of the authors (N. Miyazaki) with Dr. M. Masuda, JT-60 Project Office I, Division of Large Tokamak

Development in JAERI. Afterwards, the authors found the paper [C.3] presented in the 'International Journal of Fracture' which proposed the same method as the authors'.

References

C.1) Ishikawa H.: Finite Element Analyses of Stress Intensity Factors Using J Integral (On the Mode I and Mode II Cracks), Trans. JSME, Vol. 46, No. 401, pp. 67–76 (1980).

C.2) Private Communication from N. Miyazaki to Dr. M. Masuda, Application of Virtual Crack Extension Method to Mixed Mode Crack Problem, (1980), June 10.

C.3) Ishikawa H.: A Finite Element Analysis of Stress Intensity Factors for Combined Tensile and Shear Loading by Only a Virtual Crack Extension, Int. J. Fracture Vol. 16, R243–246 (1980).